University of New Mexico
UNM Digital Repository

9-9-2007

Growth and optimization of quantum dots-in-a-well infrared photodetectors

Ram Attaluri

GROWTH AND OPTMIZATION OF QUANTUM DOTS-IN-A-WELL INFRARED PHOTODETECTORS

BY

RAM SARAN ATTALURI

**B.E, CSE, UNIVERSITY OF MADRAS, 1999
MS, EE, UNIVERSITY OF NEW MEXICO, 2001**

COMMITTEE CHAIR: PROF. SANJAY KRISHNA

DISSERTATION

Submitted in Partial Fulfillment of the
Requirements for the Degree of

**Doctor of Philosophy
Engineering**

The University of New Mexico
Albuquerque, New Mexico

July, 2007

Dedicated to my father, Rajendra Prasad Attaluri, mother, Lakshmi Bullemma, and, sister, Lalitha Kiran

ACKNOWLEDGMENTS

I would like to thank my advisor Dr. Sanjay Krishna for believing in me and for his valuable guidance in my research. I am deeply indebted to Dr. Andreas Stintz for teaching me MBE growth and for providing guidance in my research. I would also like to thank Senthil, Jiayi, Kalyan and JB for help in processing and device characterization. I want to thank Dr. Tom Vandervalde for the useful discussions about growth and analysis of sample material and for teaching me the art of technical writing.

I would also like to thank other members of the group who provided valuable input to the research. Finally, I would like to thank the Attaluri family and to all my cousins, who have been very supportive through all these years. I would not be here if not for my father's passion for education and my family's support all through these years.

GROWTH AND OPTMIZATION OF QUANTUM DOTS-IN-A-WELL INFRARED PHOTODETECTORS

BY

RAM SARAN ATTALURI

B.E, CSE, UNIVERSITY OF MADRAS, 1999
MS, EE, UNIVERSITY OF NEW MEXICO, 2001

COMMITTEE CHAIR: PROF. SANJAY KRISHNA

ABSTRACT OF DISSERTATION

Submitted in Partial Fulfillment of the
Requirements for the Degree of

Doctor of Philosophy
Engineering

The University of New Mexico
Albuquerque, New Mexico

July, 2007

GROWTH AND OPTMIZATION OF QUANTUM DOTS-IN-A-WELL

INFRARED PHOTODETECTORS

by

Ram Saran Attaluri

B.E., CSE, University of Madras, 1999

MS, Electrical Engineering, University of New Mexico, 2001

ABSTRACT

Quantum dot infrared photodetectors (QDIPs) have been shown to be a key technology in mid and long wavelength (3-14 μm) infrared detection due to their potential for normal incidence operation and low dark current. In our research group, we have been investigating infrared detectors based on intersubband transitions in a novel InAs/In$_{0.15}$Ga$_{0.85}$As quantum dots-in-well (DWELL) heterostructure. In the DWELL structure, the InAs quantum dots are placed in an In$_{0.15}$Ga$_{0.85}$As well, which in turn is placed in a GaAs matrix. Due to the large band offset between the ground electronic state of the InAs quantum dot and conduction band edge of the GaAs barrier, thermionic emission and dark current are significantly reduced in the DWELL structure. The DWELL design also offers other advantages such as better control over the operating peak response wavelength and bias dependent tunable spectral response based on the quantum confined stark effect (QCSE). We have recently fabricated the first long wavelength quantum dot infrared photodetector (QDIP) focal plane array based on this

system and for the first time collobarators at Jet Propulsion Laboratory (JPL) have shown that QDIP performance has surpassed that of Quantum Well Infrared Photodetector (QWIP). In this work, we will investigate various methods we implemented in improving the performance of the DWELL photodetectors.

Although QDIPs based on intersubband transitions have been investigated before, there has been no careful study on the effects of Si-doping on the performance of these detectors. A careful study has been done to determine the optimal doping of the $InAs/In_{0.15}Ga_{0.85}As/GaAs$ DWELL detectors. It has been found that 3 x 10^{10} cm^{-2} is the optimal doping for the DWELL detectors. It has been observed that the spectral response, photocurrent, dark current, responsivity and detectivity (D*) increased with the amount of doping in the InAs QDs. In addition, the background limited infrared photodetector (BLIP) temperature (91K) is the highest for one electron per dot sample.

In our standard QDIPs there is only a single pass of incident light through the active region. The development of a mechanism for multiple light passes through the active region should result in a significant responsivity enhancement of QDIP detectors. One such method to create multiple light passes is to add a mirror that reflects the light back into the active region effectively developing an optically resonant cavity. In this work, we have epitaxially inserted a DBR below the QDIP device that has a broad reflectivity spectrum (i.e. 8-11μm) and designed the resonant cavity for 9.5 μm wavelength. We have observed an increase in the responsivity of the device (0.76A/W at 1.4V) relative to devices with the same active region and no mirror or cavity. Hence, we believe that the QDIP with resonant cavity and distributed Bragg reflector has improved

the performance of the device. The D* increased by a factor of three compared to the standard DWELL at a bias of 1.2 V and 77 K.

In the standard QDIP the average compressive strain in the DWELL is about 1.35% and, therefore, more number of DWELLs cannot be grown without introducing defects or dislocations. Ideally, more number of DWELLs mean more absorption, which translates to increased quantum efficiency and performance of the device. A low strain alternative design $InAs/GaAs/Al_{0.1}Ga_{0.9}As$ DWELL structure is developed which maintains approximately the same band offset between the singly degenerate ground state of the dot and the conduction band edge of the barrier. This alternative design has only (~0.35%) compressive strain in the DWELL, which allows incorporation of more DWELL layers in the active region. We observed spectrally tunable response with bias and long wave IR response at 6.2 μm and 8.4 μm. This design was also tech transferred to JPL who demonstrated a 640 × 512 infrared camera with 40 mK NEDT at 60 K. Further work is being done to fabricate FPA based on this device and compare it with the standard DWELL design.

TABLE OF CONTENTS

List of Figures

List of Tables

Chapter 1

Introduction

1.1   Infrared Radiation

Infrared radiation can be felt as heat although it cannot be seen with a human eye. All objects at room temperature emit radiation mostly concentrated at long-wave infrared. Infrared radiation from the sun is responsible, to a great extent, for heating earth, the rest being caused by visible light that is absorbed and reradiated at longer wavelengths. Infrared radiation (0.75μm to 1000μm) is the light that lies between visible and microwave portion of the electromagnetic spectrum. Figure 1.1 shows the electromagnetic spectrum. Sir Frederick William Herschel first discovered infrared radiation in 1800 by using a prism to refract sunlight and detecting the radiation through an increase in temperature recorded with a thermometer [1]. Infrared radiation is divided to many sub-bands as defined in Table 1.1.
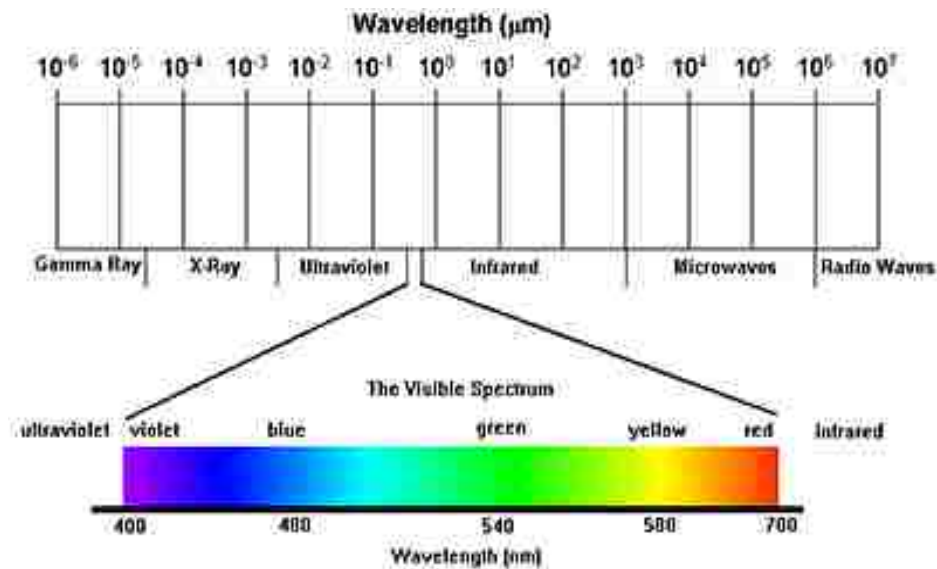
Figure 1.1: The Electromagnetic Spectrum

Sub-band	Wavelength range (μm)
Near infrared (NIR)	0.75-1.1
Short-wave infrared (SWIR)	1.1-3
Mid-wave infrared (MWIR)	3-6
Long-wave infrared (LWIR)	6-18
Very long-wave infrared (VLWIR)	18-50
Far infrared (FIR)	50-100
Submillimeter-wave (SMMW)	100-1000

Table 1.1: Sub-bands of Infrared radiation

1.2   Applications of Infrared Sensing

Infrared detection has applications in many fields of study and brings together specialty areas like optics, solid-state physics, low-noise electronics, cryogenics, statistical analysis, optical communication, astronomy, 2-D imaging, and spectroscopy. Infrared detectors have many applications ranging from military and industrial to medical and scientific, as shown in Table 1.2 [2]. The majority of activity for infrared applications has been in military and space applications. The high cost of infrared imaging systems has limited its use in commercial applications [3]. During recent years, infrared detectors have progressed from discrete detectors to large multiplexed 2-D arrays of detector pixels called focal plane arrays (FPA).

IR Technique	Military	Industrial	Medical	Scientific
Search, Track, and range	• Intrusion detection • Bomber defense • Missile guidance • Navigation and flight control • Proximity fuses • Ship, aircraft, ICBM, and mine detection • Fire control • Aircraft collision warning	• Forest fire detection • Guidance for fire-fighting missiles • Fuel ignition monitor • Locating hidden law • Violators • Monitoring parking meters • Detect fires in aircraft fuel tanks	• Obstacle detection for the blind	• Satellite detection • Space vehicle navigation and flight control • Horizon sensors • Sun followers for instrument orientation • Studies of the optical structure of the horizon
Radiometry	• Target signatures	• Detection of hot boxes on railroad cars • Noncontact dimensional determination • Process control • Measurement of the temperatures of brake linings, power lines, cutting tools, welding and soldering operations, and ingots	• Measurement of skin temperature • Early detection of cancer • Monitor healing of wounds and onset of infection without removing bandages • Remote biosensors • Studies of skin heating and temperature sensation	• Measurement of lunar, planetary and stellar temperatures • Remote sensing of weather conditions • Study of heat transfer in plants • Measurements of the earth's heat balance
Spectro-Radiometry	• Terrain analysis • Poison gas detection • Target and background signatures • Fuel vapor detection • Detection of contaminants in liquid oxygen piping	• Detection of clear-air turbulence • Analysis of organic chemicals • Gas analysis • Determination of alcohol in the breath • Discovery of leaks in pipelines • Detection of oil in water • Control of oxygen content in germanium and silicon	• Detection and monitoring of air pollution • Determination of carbon dioxide in the blood and in expelled air	• Determination of the constituents of earth and planetary atmospheres • Detection of vegetation or life on other planets • Terrain analysis • Monitor spacecraft atmospheres • Zero-G liquid level guage • Measurement of magnetic fields
Thermal Imaging	• Reconnaissance and surveillance • Thermal imaging • Submarine detection • Detection of underground missile sites, personnel, vehicles, weapons, cooking fires, and encampments • Damage assessment	• Nondestructive testing • Inspection • Locating piping hidden in walls and floors • Inspection of infrared optical materials • Detect and display microwave field patterns • Study efficiency of thermal insulators	• Early detection and identification of cancer • Determination of the optimum site for an amputation • Localization of the placental site • Studies of the efficiency of arctic clothing • Early diagnosis of incipient stroke	• Earth resources surveys • Locate and map the gulf stream • Detect forest fires from satellites • Study volcanoes • Detect and study water pollution • Locate crevasses • Sea-ice reconnaissance • Petroleum exploration
Reflected Flux	• Night driving • Carbine firing • Intrusion detection • Area surveillance • Camouflage detection • Station keeping • Docking and landing	• Industrial surveillance and crime prevention • Examination of photographic film during manufacture • Detection of diseased trees and crops • Travelling matter photography • Automatic focusing of projectors	• Measurement of papillary diameter • Location of blockage in a vein • Monitoring eye movements • Study of nocturnal habits of animals • Examination of the eye through corneal opacities • Monitor healing processes	• Detection of forgeries • Determine thickness of epitaxial films • Determination of the surface constituents of the moon and the planets • Gem identification • Analysis of water quality • Detection of diseased crops
Cooperative source	• Terrestrial communications • Command guidance for weapons • Countermeasures for infrared systems • Range finding • Drone command link • Intrusion detection	• Intrusion detection • Automobile collision prevention • Traffic counting • Radiant heating and drying • Data link • Intervehicle speed sensing • Aircraft landing aid • Cable bonding	• Ranging and obstacle detection for the blind • Heat therapy	• Space communications • Understand the mechanism of animal communication • Peripheral input for computers • Study the nocturnal habits of animals • Terrain illumination for night photography

Table 1.2: The IR applications matrix, spread over the Industrial-Scientific-Medical and Military (ISM-M) horizons [2].

1.3   Principles of Photodetection

In semiconductors, when light with photons of sufficient energy is incident on the surface of the semiconductor the photon can be absorbed and electron-hole pairs may be created. The energy of a photon must be greater than or equal to the band gap of the semiconductor material in order for absorption to take place and to promote the electron from valence band to conduction band. The energy of the photon can be related to the frequency or wavelength of the light as follows:

$$E = h\upsilon = \frac{hc}{\lambda}$$
, (1)

where E is the energy of the photon, h is the planck's constant, v is the optical frequency of the photon, c is the speed of light and λ is the wavelength at which the lowest energy photon can be detected and whose energy is equal to the band gap.

An important figure of merit, for assessing the performance of the detector, is the quantum efficiency (η). It is the ratio of the number of electrons generated to the number of photons incident on the detector. In other words, it can be defined as the efficiency of converting a photon to an electron and is normally expressed in percentage units. An ideal photodetector would have a quantum efficiency of one. In reality, all photodetectors have quantum efficiency less than one, as shown in Figure 1.2. As seen in the curve, λ_{cutoff} is the wavelength of the minimum energy photon that can be absorbed beyond which the quantum efficiency is zero.
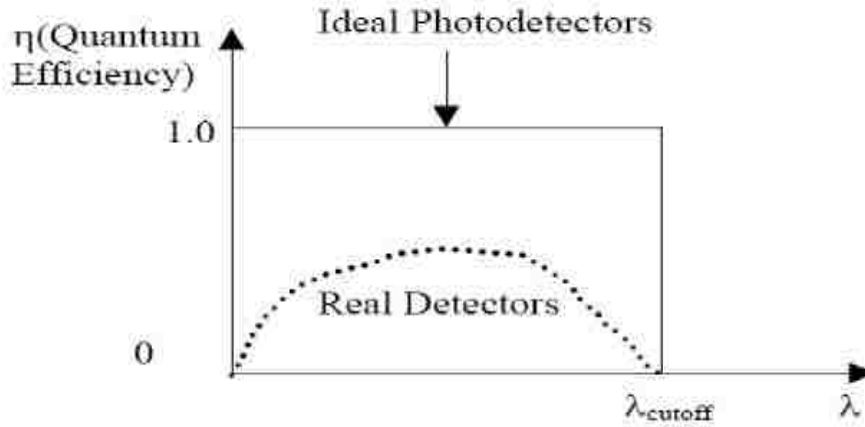
Figure 1.2: Quantum efficiency versus wavelength

1.4   Types of Infrared Detectors

Most of the present day infrared detectors can be classified into two types:

photovoltaic detectors and photoconductors.

1.4.1 Photovoltaic Detectors

Photovoltaic detectors consist of a p-n junction or a p-i-n junction whose

depletion region is sensitive to infrared radiation and generates a current when

illuminated with infrared light. The photogenerated current (i_{ph}) is given by [6]:

$$i_{ph} = \eta \phi_q q \quad , \tag{2}$$

where η is the quantum efficiency, φ_q is the photon flux, which is the number of incident

photons per unit time, and q is the charge of the electron. The diode equation is modified

by the addition of the photogenerated current as follows [6]:

$$i = i_o \left(e^{qv/bkT} - 1 \right) - i_{ph} \quad , \tag{3}$$

where i_o is the reverse saturation current, v is the voltage applied across the photodiode, b

is the non-ideality factor, k is the boltzmann's constant and T is the temperature. Most of

the photovoltaic detectors operate in the reverse bias regime as the depletion region width increases in that bias regime and therefore generate more current when illuminated. Photovoltaic detectors have high quantum efficiencies ranging from 45% to 86% which explains why they are frequently used in state-of-the-art detectors [4] [5].

1.4.2 Photoconductors

Photoconductors operate on the principle that the resistance of the detector changes when illuminated with light. The resistance is inversely proportional to the photon flux and, therefore, the conductivity of the detector increases when light is incident upon it. Photoconductors can be classified into intrinsic and extrinsic on the basis of how the detector is doped. Intrinsic photoconductors (e.g. HgCdTe) do not have any external dopants and depend on the intrinsic carrier concentration of the semiconductor. The cut-off wavelength of the intrinsic photoconductors depends on the energy band gap of the semiconductor material because the photon must have sufficient energy to cause the electron to move from the valence band to the conduction band. Intrinsic photoconductors have high quantum efficiencies ranging from 50% to 60%.

Extrinsic photoconductors are doped with external dopant species (e.g. Si is a dopant for InAs) and are usually used to obtain a longer wavelength response toward the infrared region (i.e. smaller band gap). In extrinsic photoconductors, the photons are absorbed by the carriers in the dopant states and get promoted to the conduction band or valence band depending on the type of dopant (i.e n-type for donors and p-type for acceptors). These photoconductors suffer from low operating temperatures due to smaller activation energies. For detector materials with small energy bandgaps, electrons can be thermally excited into the conduction band (dark current). The photogenerated electrons

6

are the desired signal, not the thermally generated electrons. Based on the Boltzmann's distribution, the population of the energy levels follows an exponent, exp $\{-\varepsilon_g/kT\}$; as ε_g becomes smaller, while temperature T constant, the number of thermally generated electrons increases exponentially [6]. The detector has to be cooled to a cryogenic temperature to prevent the thermally generated electrons from dominating the photo electron generation process. In addition, extrinsic photoconductors also suffer from low QEs when compared with intrinsic photoconductors due to low absorption cross section resulting from the low volumetric density of the extrinsic dopant species compared to the host material. Extrinsic photoconductors have QEs ranging between 30 and 40%. Quantum dot infrared detectors (QDIPs) and quantum well infrared detectors (QWIPs) described in detail later are good examples of extrinsic photoconductors. In this dissertation, we are mainly concerned about a device that is a hybrid of these two technologies called dots in a well (DWELL) infrared detector QDIPs.

1.5   Figures of Merit for Photoconductors

Figures of merit are mainly used to characterize or quantify the performance of the photodetectors. While there are many figures of merit; we will discuss those that are relevant to present day photodetectors.

1.5.1 Responsivity

Responsivity is the ratio of the output current generated per input optical power incident on the detector measured in Amperes/Watt. It is related to the internal QE through the following equation [6]:

$$R = \frac{\eta q \lambda}{hc} G , \qquad (4)$$

where η is the internal quantum efficiency, q is the charge of electron, λ is the wavelength

of the photon, h is planck's constant, c is the speed of light, and G is the photoconductive

gain. Photoconductive gain is the fraction of thermally or photogenerated carriers that

reach the collecting contacts. It is the ratio of carrier lifetime to carrier transit time. This

expression of responsivity is related to the wavelength of the photon and, therefore, is

called spectral responsivity. On the contrary, the blackbody responsivity takes into

account all wavelengths of the spectral responsivity and is related to the blackbody

temperature. The blackbody responsivity is a more comprehensive measure for a detector

and is given by [6]:

$$R_i = \frac{I_o}{\displaystyle\int_{\lambda_1}^{\lambda_2} \frac{R(\lambda)}{R(\lambda_c)} L_e(\lambda,T) \frac{A_s A_d}{r^2} t F_F \, d\lambda} , \qquad (5)$$

where I_o is the output current produced by the detector (Amps), $R(\lambda)/R(\lambda_c)$ is the

normalized spectral response, $L_e(\lambda,T)$ is the blackbody radiance, A_s is the blackbody area,

A_d is the detector area, t is the transmittance, F_F is the optical chopper form factor for

conversion of peak-to-peak to rms, and r is the distance between the blackbody source

and the detector. The limits of the responsivity spectrum are represented by λ_1 and λ_2. The

blackbody radiance as a function of wavelength, λ, and blackbody temperature, T, and is

given by Planck's law as follows [6]:

$$L_e(\lambda,T) = \frac{2c^2 h}{\lambda^5 (e^{\frac{hc}{k\lambda T}} - 1)} \left[\frac{watt}{cm^2 \, sr \, \mu m} \right] . \qquad (6)$$

1.5.2 Photocurrent and Dark Current

Photocurrent, or the photogenerated current, is the current that is generated due to absorption of photons. Dark current is the current that is generated thermally or due to phonon interaction and is present when no light is incident on the detector. When the photocurrent is greater than the dark current, the detector is background limited. The temperature at which this happens is called BLIP, or background limited infrared performance, and it is a good measure of the operating temperature of the detector.

1.5.3 Detectivity

Detectivity (D*) is a measure of the signal-to-noise-ratio of the detector and is normalized to the detector area. Detectivity is the most important figure of merit for all photodetectors as it takes into consideration both the signal and noise performance of the detector. Since it takes into account the blackbody responsivity, the detectors response at all wavelengths is considered. Therefore, it is also the most comprehensive figure of merit for a detector. Greater the detectivity, the higher the sensitivity of the detector. The unit of detectivity is cm Hz$^{1/2}$/W or Jones. The detectivity is given by the following equation [6]:

$$D* = \frac{\sqrt{A_d \, \Delta f}}{i_n} R_i \, , \qquad (7)$$

where A_d is the area of the detector, Δf is the noise equivalent bandwidth, and i_n is the noise current. The noise current is a sum of many sources of noise (i.e. generation-recombination noise, shot noise, 1/f noise….etc) and is given by the equation:

$$i_n^2 = i_{G-R}^2 + i_j^2 + i_{1/f}^2 + \Lambda \, \Lambda \, , \qquad (8)$$

The most dominant source of noise in a photoconductor (i.e. particularly in QDIP) is the generation-recombination noise. It arises due to the fluctuations in the generation and recombination processes occurring in the active region of the detector. The fluctuations are caused due to the random nature of the processes occurring in the detector and can be specified by Poisson statistics as follows [6]:

$$i_{G-R} = 2qG\sqrt{\eta E_q A_d \Delta f + g_{th} A_d \Delta f l_x} \, , \tag{9}$$

where G is the photoconductive gain, E_q is the photon irradiance, g_{th} is the thermal generation factor and l_x is the thickness of the detector. The second term, which is due to the thermal generation of carriers, can be neglected as the detector is cooled.

The other source of noise is thermal, or Johnson noise, and is usually caused by the random motion of carriers with average energy kT in a resistive element. As most photoconductors are generally operated at cryogenic temperatures, Johnson noise is not so prominent. This noise is dominant at high frequencies and high temperatures. It is given by the following equation [6]:

$$i_j = \sqrt{\frac{4kT\Delta f}{R}} \, , \tag{10}$$

The dominant noise at low frequencies is 1/f noise, or flicker noise, which is caused by surface and interface defects, or traps, in the semiconductor material.

1.6   Quantum Dots

A quantum well (QW) is a thin layer which can confine electrons or holes in the dimension perpendicular to the layer surface, while the movement with in the layer is not restricted [7]. A QW is formed when a lower band gap material is sandwiched between higher band gap materials. Figure 1.3 illustrates the band structure of a GaAs/AlGaAs-

based QW [8]. As seen in the figure, the electron is confined in the z-direction, or normal to the surface of the layer, by the QW. As a layer thickness approaches de-Broglie wavelength (i.e. about 10 nm), quantum effects can be seen. Therefore, usually the QW thickness is in the order of 1 to 15 nm. Similarly, in the quantum dot the carrier is confined in all three dimensions.
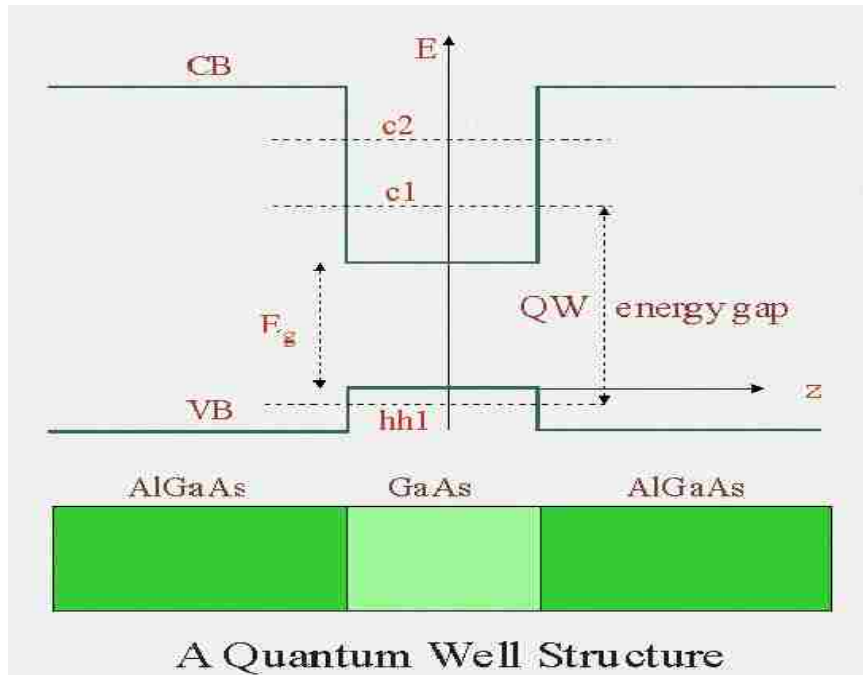
Figure 1.3: Band structure of a GaAs/AlGaAs Quantum well

The change in confinement can be better understood if we compare the density of states for bulk (0-dimension), QW (1-dimension), Quantum dash or wire (2-dimensions) and QD (3-dimensions). As seen in Figure 1.4, the density of states function for bulk is continuous and proportional to the square root of energy [9]. The density of states decreases for QW compared to the bulk and is a step function. For the quantum wire the density of states further decreases compared to the QW. For QDs, the density of states

decreases compared to a quantum wire and is a delta function in energy. For real devices made of QDs, however, the density of states has a line broadening due to variations in dot size.

The low density of states and small size of the dots means that fewer carriers are needed to invert the carrier population, which results in low threshold current density and high characteristic temperature when incorporated as active region in a laser. In terms of detector, the absorption of the dots can be easily saturated due to the finite density of states.
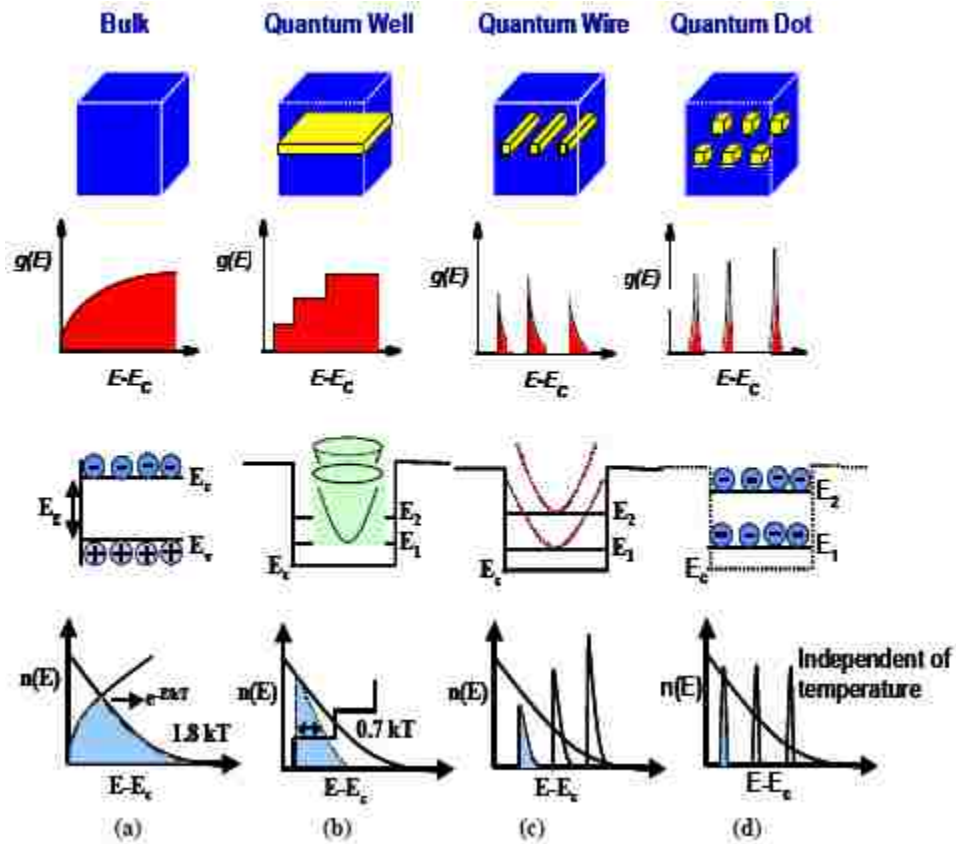
Figure 1.4: Density of states, bandstructure and carrier distribution for (a) bulk, (b) quantum well, (c) quantum wire and (d) quantum dots.

1.7   Formation of Self-Assembled Quantum Dots

There are several ways to form QDs, Self-assembly using epitaxy is the most efficient technique to achieve coherently strained QDs. The self-assembly process can be understood by reviewing the three modes of heteroepitaxial growth. As seen in Figure 1.5, when the strain between the epitaxial layer and the substrate is minimal it results in two-dimensional growth, called as Frank-van der Merwe mode. The strain that is referred here is compressive strain which is caused by deposition of an epitaxial layer with a larger lattice constant than the substrate and, therefore, are lattice mismatched. As the strain increases, beyond a certain critical thickness of the epitaxial layer, it is energetically favorable to increase surface area by forming 3D islands than by relaxing the strain through dislocation generation. This growth regime is referred to as Stranski-Krastanow mode of growth and starts initially with 2D growth followed by 3D island growth [10]. This is the growth regime for formation of InAs QDs on a GaAs substrate. The critical thickness for transition from 2D layer-by-layer growth to 3D island formation is 1.6 - 1.7 monolayers (MLs). If the lattice mismatch between the epitaxial layer and the substrate is very high, there is direct formation of 3D islands, called Vollmer-Weber growth [11]. Most of the present day QDIPs are grown using Stranski-Krastanov process using molecular beam epitaxy (MBE) or metal organic chemical vapor deposition (MOCVD).

Figure 1.5: Three modes of strained heteroepitaxial growth.

1.8 Quantum Dot Infrared Photodetectors (QDIPs)

The three-dimensional confinement of QDs helps in localization of carriers reducing the thermionic emission which in turn lowers the dark current [12] - [15]. The intersubband energy level spacing in the QDs is greater than the phonon energy and, therefore, reduces the phonon scattering, which is a dominant scattering mechanism in bulk and QWs. This is the reason for long carrier relaxation times in QDIPs, which in turn increases the photoconductive gain. The responsivity and detectivity are also increased due to the increase in gain and photocurrent [12] - [15]. In addition, QDIPs are sensitive to normal incidence radiation, which is not possible in QWIPs, due to polarization selection rules, and requires specialized gratings to direct the radiation into the detector. The QDs are normally doped to about than 1-2 electrons per dot in order to prevent carriers from occupying the excited state which will increase the dark current. The thickness of the barriers surrounding the quantum dots, the doping concentration, and the number of quantum dot layers are important parameters to consider while designing a QDIP.

QDIPs suffer from low QE due to low absorption cross section resulting from low density of QDs and finite spacing between the dots [16]. This thesis discusses different ways to improve the quantum efficiency and other performance parameters like responsivity, detectivity, operating temperature, of QDIPs based on dots-in-well (DWELL) design.

1.9 DWELL Design

In the DWELL design, the active region consists of 2.4 MLs of InAs QDs placed in an 11nm $In_{0.15}Ga_{0.85}As$ QW sandwiched between 50 nm thick GaAs barriers, which in turn is placed in a GaAs matrix. The DWELL design is shown in Figure 1.6. As seen in the figure, there is a large conduction band offset (i.e. 250 meV) between the ground electronic state of the InAs QD and the conduction band edge of the GaAs barrier, which reduces the thermionic emission and therefore low dark current [17]. Due to low dark current, QDIPs are expected to have higher operating temperatures than QWIPs. The total band offset is calculated from photoluminescence (PL) spectrum and using the 60-40% split. The excited state is obtained from spectral response and theoretical modeling [17]. The spacing between the ground electronic state and excited state is found to be about 50 -60 meV [18]. The PL spectrum of the 10-period InAs/ $In_{0.15}Ga_{0.85}As$ dots-in-well (DWELL) QDIP is shown in Figure 1.7.
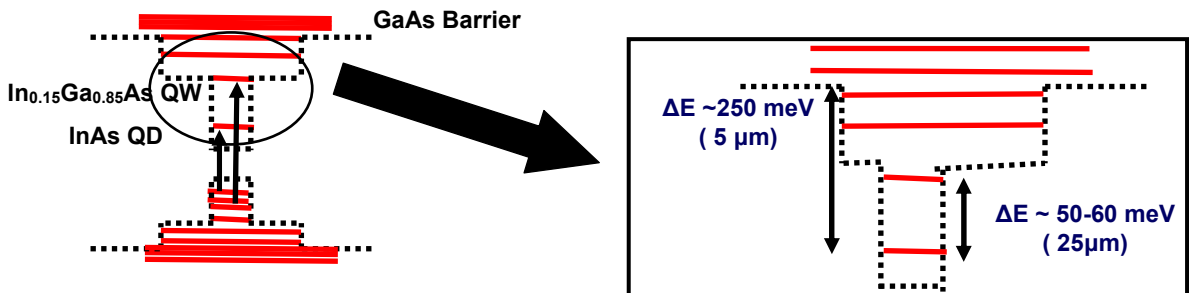
Figure 1.6: Band structure of InAs/$In_{0.15}Ga_{0.85}As$ DWELL

The PL from the ground state of the valence band and conduction bands is 0.976 eV and from the excited states is 1.026 eV. The PL at 1.065 eV might be from the excited states in the InAs QD. The PL is measured with a He-Ne laser using a grating spectrometer and an InGaAs detector. The desired wavelength can be tuned by changing the thickness of the $In_{0.15}Ga_{0.85}As$ QW. Since the QDIP based on a DWELL design mainly operates on intersubband transitions, if the thickness of the QW changes, then the energy level spacing changes and, therefore, the absorption can be tuned to the desired wavelength. In addition, bias tunable spectral response is observed in QDIPs based on DWELL designs due to the exploitation of the asymmetry of the band structure by quantum confined stark effect (QCSE) [19].
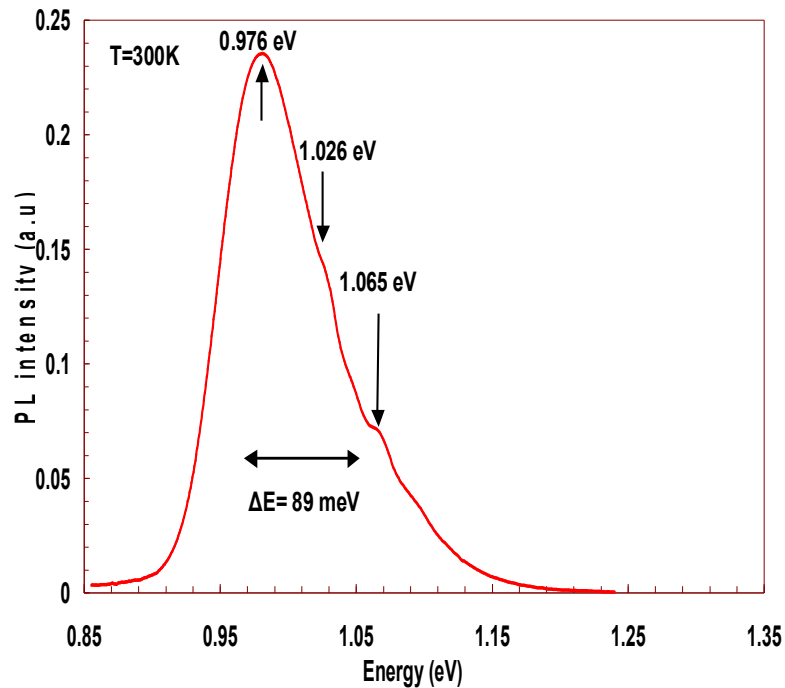
Figure 1.7: Photoluminescence spectrum of a 10-period InAs/ $In_{0.15}Ga_{0.85}As$ dots-in-well (DWELL) Quantum dot infrared Photodetector.

Infrared detectors based on DWELL design primarily work on bound-to-bound transitions from the ground electronic state of the InAs QD to the $In_{0.15}Ga_{0.85}As$ QW and bound-to-continuum transition from the ground electronic state of the InAs QD to a state in the GaAs barrier as illustrated in Figure 1.8. Depending on the bias, one of the transitions is observed in the spectral response for the detector.

Bound to Bound
Bound to Continuum

GaAs   GaAs

$In_{0.15}Ga_{0.85}As$ $In_{0.15}Ga_{0.85}As$
60 Å   **50 Å**

InAs QDs
2.4 MLs
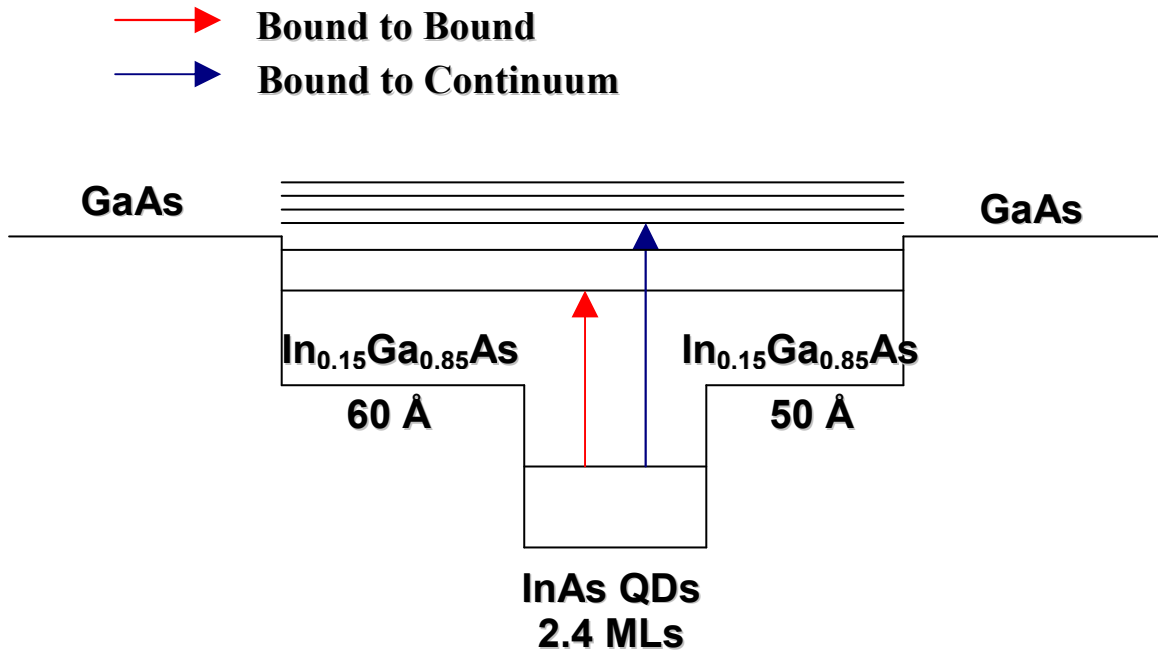
Figure 1.8: Various transitions in the dots-in-well (DWELL) QDIP

1.10 Overview of dissertation

The main objective of this research is to increase the operating temperature and detectivity (D^*) of the quantum dots-in-well infrared photodetectors. In this investigation various methods have been applied using growth and design modifications to improve the quantum efficiency, detectivity, and operating temperature of the detector.

The doping in the QDs is an important parameter for QDIPs as increasing doping has been proved to increase the dark current and hence noise of the detector. Chapter 2 discusses the research that has been done to find the optimal doping for the InAs/In$_{0.15}$Ga$_{0.85}$As quantum dots-in-well infrared photodetectors in order to decrease the dark current and enhance the performance of these detectors.

Chapter 3 discusses the investigation done to improve the quantum efficiency of the InAs/In$_{0.15}$Ga$_{0.85}$As quantum dots-in-well infrared photodetectors by placing the active region in a resonant cavity and using a bottom distributed bragg reflector (DBR) mirror and top air/semiconductor interface to trap light in the active region. This way multiple passes of light can be attained and therefore more absorption in the quantum dots which will increase the QE of the detector.

In Chapter 4, a new alternative DWELL design (InAs QDs placed in a GaAs QW) is investigated. In the standard design (InAs QDs placed in an In$_{0.15}$Ga$_{0.85}$As QW) the average strain is very high and many DWELL layers cannot be grown without introducing dislocations, which will lower the performance of the detectors. Hence, the new design is for increasing the number of DWELL layers in order to increase the overall absorption, which in turn increases the photocurrent and detectivity. These three approaches have significantly improved the performance of DWELL detectors.

---

[1] W. Herschel, Phil. Trans. R. Soc. Lond., 90:255, 1800.

[2] Richard D. Hudson Jr., Infrared System Engineering, John Wiley & Sons (1969).

[3] Sunil Raghavan, Intersubband Quantum dots-in-a-well infrared photodetectors, University of New Mexico, 2003.

[4] Phillips J, 2002 J. Appl. Phys., (91) 4590.

[5] Sidorov Yu G, Dvoretsky S A, Yakushev M V, Mikhailov N N, Varavin V S and Liberman V I, 1997 Thin Solid Films, (306)253.

[6] E.L Derniak and G.D. Boreman, Infrared Detectors and Systems, John Wiley & Sons, New York, 1996.

[7] http://www.rp-photonics.com/quantum_wells.html

[8] http://people.deas.harvard.edu/~jones/ap216/images/bandgap_engineering/ bandgap_engineering.html

[9] Sanjay Krishna, Optoelectronic Properties of Self-Assembled InAs/InGaAs Quantum Dots.

[10] I.N Stranski, and L. Krastanow 1937 Sitzungsberichte d. Akad. D. Wissenschaften in Wien, Abt. IIb, 146.

[11] C. Ratsch , and A. Zangwill, 1993 Surf. Sci., 293, 123.

[12] Shiang-Feng Tang, Cheng-Der Chiang, Ping-Kuo Weng, Yau-Tang Gau, Jiunn-Jye Luo, San-Te Yang, Chih-Chang Shih, Shih-Yen Lin, and Si-Chen Lee, IEEE Photonics Tech. Lett., 18(8), 2006.

[13] V Ryzhii, Semicond. Sci. Technol. **11** (1996) 759–765.

[14] L. Fu, H. H. Tan, I. McKerracher, J. Wong-Leung, C. Jagadish, N. Vukmirović and P.Harrison, J. Appl. Phys. 99, 114517 (2006).

[15] Mohamed B El Mashade, M Ashry and A Nasr, Semicond. Sci. Technol. 18 (2003) 891–900.

[16] S. D. Gunapala, S. V. Bandara, C. J. Hill, D. Z. Ting, J. K. Liu, S. B. Rafol, E. R. Blazejewski, J. M. Mumolo, S. A. Keo, S. Krishna, Y. C. Chang, and C. A. Shott,

Proc. SPIE Vol. 6206, 62060J (2006).

[17] A. Amtout, S. Raghavan, P. Rotella, G. von Winckel, A. Stintz, and S. Krishna, J. Appl. Phys. 96(7), 3782 (2004).

[18] S. Krishna, S. Raghavan, G. von Winckel, A. Stintz, G. Ariyawansa, S. G. Matsik, and A. G. U. Perera, Appl. Phys. Lett., Vol. 83, No. 14, 2746, October 2003.

[19] U. Sakoğlu, J. S. Tyo, and M. M. Hayat et al, J. Opt. Soc. Am. B **21**, 7 (2004).

Chapter 2

Influence of Si-Doping on the Performance of InAs/In$_{0.15}$Ga$_{0.85}$As DWELL Infrared Detectors

2.1   Introduction

Theoretically, QDIPs are predicted to have low dark-current due to 3D confinement. Moreover, as a result of low electron-phonon scattering high responsivity, detectivity and operating temperatures are expected. The primary motivation for this research has been to optimize and improve the performance (responsivity, detectivity and operating temperatures) of DWELL-based photodetectors by varying important design parameters such as doping of QDs, increasing the thickness of the active region and increasing the quantum efficiency of the detector.

It has been shown that a decrease in doping leads to low dark current [1]. There have been reports from various groups about undoped QDIPs and QDIPs doped with 2e/dot [2,3,4]. One group has investigated the effect of incorporation of dopants in the dots, above the dots and below the dots [5]. Very few groups, however, have done research on finding the optimal doping for QDIPs. It is a crucial design parameter as a change in doping level is associated with increase in the dark current and noise which lowers the detectivity.   In this work, we have investigated the optimal doping for the InAs/In$_{0.15}$Ga$_{0.85}$As DWELL infrared photodetector [6] [7].

2.2 Growth

A series of DWELL samples with varying doping densities from (undoped–6 x 10^{10} cm^{-2}) were grown in a VG Semicon (V-80) Molecular Beam Epitaxy (MBE) reactor. The DWELL structure consists of 2.4 MLs of InAs quantum dots QDs embedded in a 110 Å $In_{0.15}Ga_{0.85}As$ QW which in turn is placed in a GaAs matrix. The five different samples that are grown in the order of increasing sheet doping concentration are A (undoped), B (0.75 x 10^{10} cm^{-2}), C (1.5 x 10^{10} cm^{-2}), D (3 x 10^{10} cm^{-2}) and E (6 x 10^{10} cm^{-2}). The complete design of the InAs/$In_{0.15}Ga_{0.85}As$ DWELL infrared photodetector is shown in Figure 2.1. The growth rates for InAs and GaAs used for growing the DWELL layers are 0.053 ML/s and 0.3 ML/s. For growing the barrier, top and bottom contact layers another Ga cell fixed at 0.7 ML/s is used. The growth rates are calibrated before the growth using x-ray diffraction (XRD) and reflection high energy electron diffraction (RHEED). The DWELL structure is grown on a 2" diameter GaAs semi-insulating substrate. Before growth the oxide on the substrate is desorbed at a temperature of 650° C for 10 minutes. The temperature is measured using a calibrated infrared pyrometer. After the oxide desorption a GaAs buffer layer of thickness 2000 Å is grown to smoothen the surface of the substrate. After the growth of 5000 Å GaAs bottom contact layer doped with Si (n = 2 x 10^{18} cm^{-3}) and 500 Å GaAs barrier there is a 600 sec As interrupt to lower the substrate temperature to 470° C for the growth of the DWELL layers. At the end of 600 sec As interrupt 0.716 monolayers (MLs) of InAs seeding layer is deposited to prevent a compositional gradient for the $In_{0.15}Ga_{0.85}As$ QW layers which is determined using experiments [8,9]. After the deposition of the InAs seeding layer the first part of the 110 Å $In_{0.15}Ga_{0.85}As$ QW of which 50 Å is grown and then 1.083 MLs of InAs wetting layer

22

is grown. Following the deposition of the InAs wetting layer 0.6 MLs of InAs QDs doped with Si (0 - 6 x 10^{10} cm^{-2}) are grown. The bulk doping level was measured using Hall measurements in thick GaAs films. The sheet dopant density was determined by multiplying the thickness of the film when the dopant shutter was open with the bulk doping level. The dot density was determined to be 1.1 x 10^{11} cm^{-2} from an independent AFM sample. In order to provide the carriers in the dots, the dots were doped after the growth of the wetting layer. After the deposition of 1.8 MLs of InAs, the dopant shutter was opened and the remaining 0.6 MLs of InAs was doped. The sheet doping concentration is scaled to an equivalent volume concentration with respect to GaAs. We estimate the background concentration for bulk InAs to be n=2 x 10^{16} cm^{-3}, which for a nominal thickness of 6Å, corresponds to a sheet concentration of 1.2x10^9 cm^{-2}. The InAs QDs are then capped with the remaining In$_{0.15}$Ga$_{0.85}$As QW which is 60 Å thick. After the growth of In$_{0.15}$Ga$_{0.85}$As QW, 3 MLs of GaAs are deposited at the same temperature for an abrupt interface [9]. Immediately after the growth of GaAs layer a 180 sec As interrupt is placed to increase the temperature to 590° C for the growth of 492 Å GaAs barrier. After the growth of the GaAs barrier the DWELL structure is again repeated for a total of 12-periods and then 2000 Å n$^+$-GaAs (n = 2 x 10^{18} cm^{-3}) top contact layer is grown.
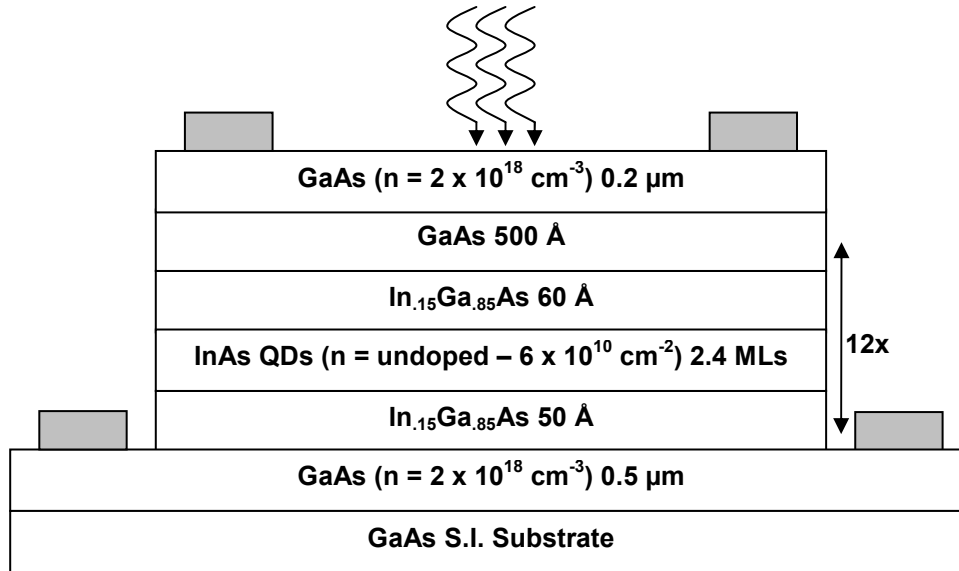
Figure 2.1: Schematic of 12-period InAs/In.15Ga.85As DWELL

infrared photodetector.

2.3   Device Fabrication

Device fabrication is done in a class-100 cleanroom where 400 μm x 400 μm mesas were defined using photolithography, metal evaporation and dry etching techniques. The processing of the photodetector consisted of five steps. In the first step the top contact is defined using photolithography. An image reversal photoresist (AZ5214E-IR) is used for exposure and AZ400K is used as the developer. In the second step the top contact (Ge/Au/Ni/Au) is deposited using metal evaporation followed by metal liftoff where the sample is soaked in acetone to remove metal from parts of the sample where it is unnecessary. In the third step, the mesa is defined using photolithography. During this step AZ4330 photoresist is used for exposure and AZ400K is used as a developer. After the third step, the device goes through a dry etch process in an inductively coupled plasma etch system such that the bottom contact layer is reached and then the bottom

contact (Ge/Au/Ni/Au) is deposited. The final step consists of annealing the contacts using rapid thermal annealing under N_2 flow at 400°C for 45 seconds.

2.4   Device Characterization

Spectral response measurements were performed at 30 K using a Nicolet 870 FTIR spectrometer. The photoresponse spectra at V=+2.8V shown in Figure 2.2. Asymmetry with respect to bias polarity was observed and has been previously reported [10]. The bias value (+2.8V) was the maximum voltage at which all samples showed significant spectral response magnitude. It can be seen that the photoresponse of the detectors increases with the amount of Si doping in the QDs, which is expected due to the increased number of carriers available for photoexcitation. For the sample with the highest doping (Sample E), there is a slight decrease in the photoresponse possibly due to occupancy of the higher lying excited states. Ideally we would have this trend to occur after the saturation of the singly degenerate ground state of the dot (2 electrons), but residual doping from the $InAs/In_{0.15}Ga_{0.85}As$ layers may provide additional carriers that occupy the ground state. It should be noted that there might be a statistical variance in the doping distribution among the QDs and not all QDs have two electrons per dot doping. For this reason, the ground electronic state of some of the QDs might be filled by carriers from the contact layers when a bias is applied. This is evident from the fact that even in the undoped sample (sample A), there was an appreciable spectral response (Fig. 2.2). This trend was also observed in the measured photocurrent when the devices were illuminated by a 300K scene under F1.7 conditions (Fig. 2.3). The inset to Fig. 2.3 shows the experimental set up for the photocurrent measurement.
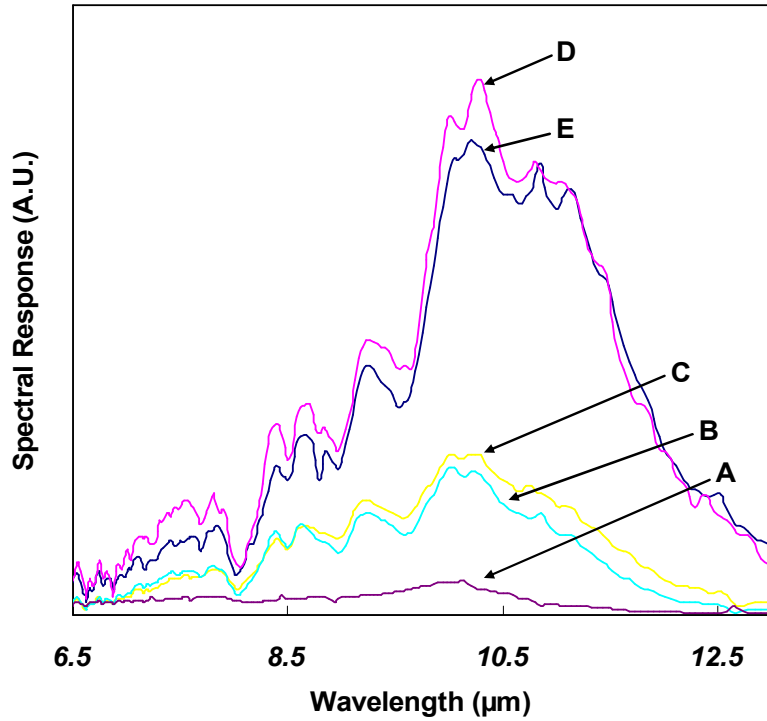
Figure 2.2: Low temperature spectral response data for samples A-E with Si doping concentrations undoped to 6 x 10^{10} cm^{-2}. All the spectra were taken at T=30K at a bias of V_b=+2.8V.
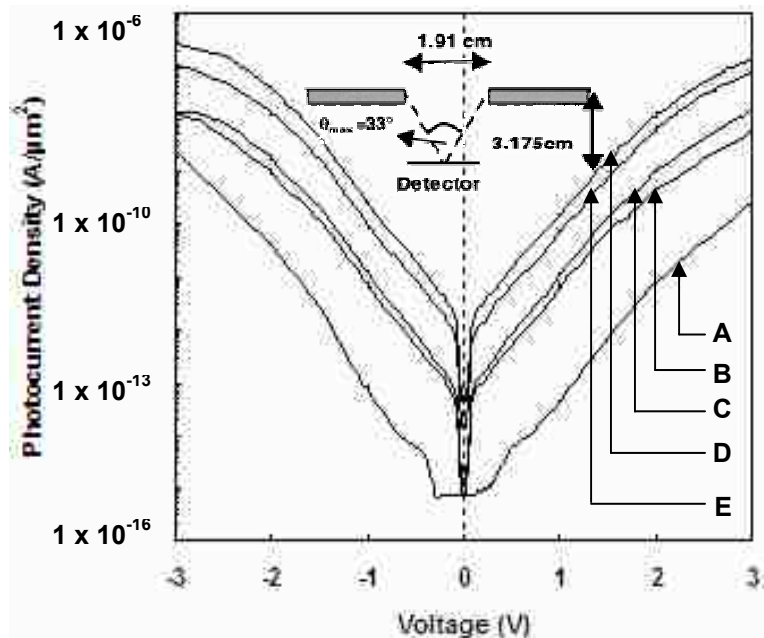
Figure 2.3: Comparison of Photocurrent densities for samples undoped – 6 × 10^{10} cm^{-2} at T=70K

The measurement of dark current density for samples A-E is shown in Figure 2.4. The dark current density increased with the amount of doping. Sample E has the highest dark current density compared to other samples. The increase in dark current density can be attributed to increased availability of free carriers due to thermionic emission. This effect has been observed in QWIPs too [11]. The dark current density of the undoped sample is lower than sample E by two orders of magnitude signifying the importance of doping on the performance of the detectors. It can be concluded that the dark current (noise) and photocurrent (signal) increase with the amount of doping; however, the figure of merit for the optimal ratio is background limited infrared photodetector (BLIP) which is the temperature at which the dark current is equal to the photocurrent. The higher the BLIP temperature, the better the detector. The BLIP temperatures for various samples are shown in Figure 2.5. The BLIP temperatures are measured while viewing a 300K blackbody under F1.7 conditions (bias -4 to +4V). It is interesting to note that sample D (3×10^{10} cm^{-2}) has the highest BLIP temperature (91K). The reason sample D has the highest BLIP temperature is that it has the optimal signal to noise ratio compared to other samples.
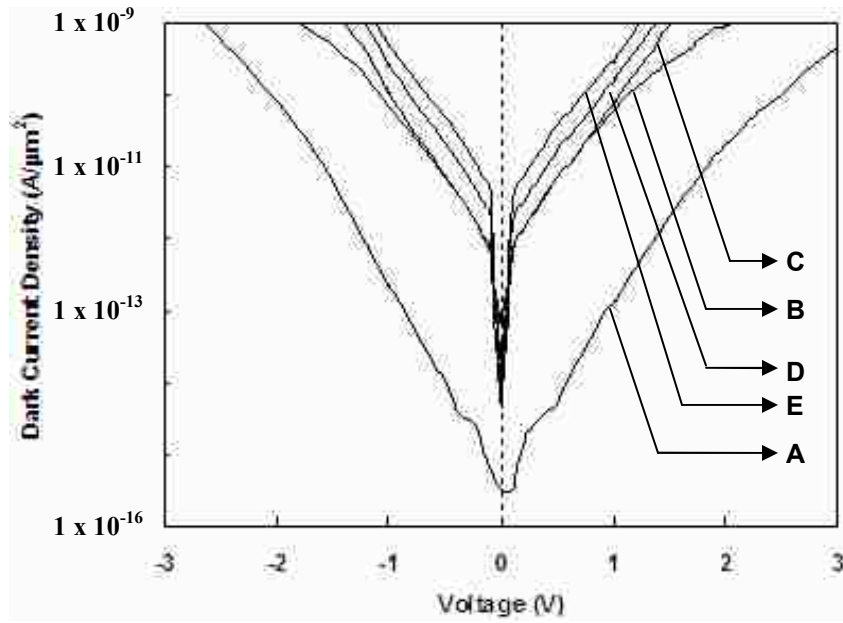
Figure 2.4 Comparison of dark current densities of samples A-E at T=70K
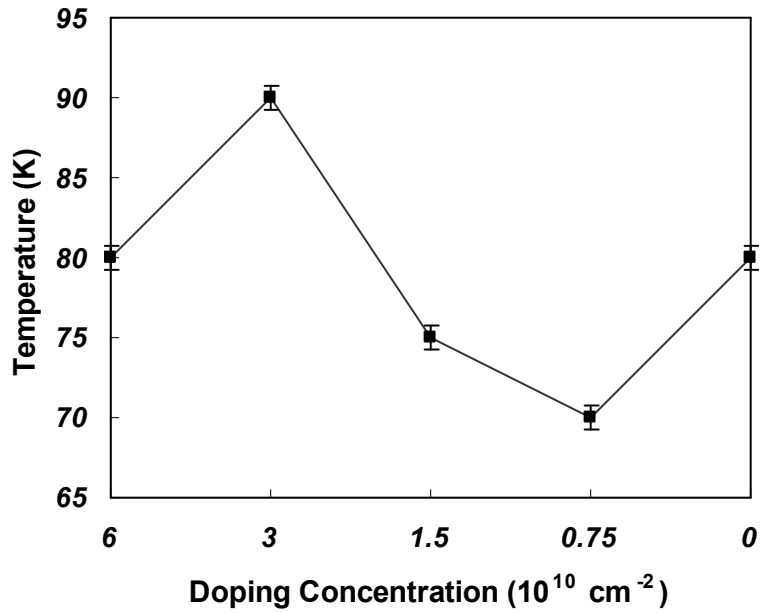
Figure 2.5: BLIP temperatures for samples A-E

One important point to note is that the photocurrent and spectral response of samples B&C are very similar while being an order of magnitude higher than samples D&E, which are also similar. We initially thought this was probably due to the filling of the ground states in samples B & C leading to a large number of carriers available for the photoexcitation in the excited state. However, a detailed analysis of the activation energy and a lack of spectral shift did not corroborate this hypothesis. The fact that this behavior is visible in two independent measurements (spectral response and photocurrent density) suggests a dramatic dependence on the doping level. This trend could be due to the interplay between filling of the energy levels and the "allowable" transitions in the DWELL system although it is very difficult to theoretically determine these selection rules.

Calibrated radiometry measurements were undertaken using a 800K blackbody and an optical chopper to determine the responsivity of the detectors. The measurement setup is shown in Figure 2.6. The setup consists of a 800K blackbody, an optical chopper rotating at 400 Hz and a sample mounted in a low noise cryostat connected to a current amplifier. The output from the current amplifier is connected to the input of a fast fourier transform (FFT) analyzer. Also the chopper is connected as a trigger to the FFT analyzer. The output current signal from each sample is measured from the analyzer and using the spectral response data the responsivity is deduced using the following equation:

$$R_P = \frac{I_{Sig}}{\int_{\lambda 1}^{\lambda 2} \frac{f(\lambda)}{f(\lambda_P)} \cdot E(\lambda, T) \cdot A_d \cdot FF \cdot d\lambda},$$

where I_{Sig} is the measured value and $E(\lambda, T)$ is the radiation power incident on the device as a function of wavelength and temperature. $f(\lambda)$ and $f(\lambda_p)$ are the respective

29

spectral response data at λ and peak wavelength λ_p and A_d is the area of the detector. Form factor (FF) is dependent on the geometries of the blackbody, cryostat and the chopper. It is also dependent on the distance between the blackbody and the sample in the cryostat. The measured responsivity at 77K for the samples A, D and E is shown in Figure 2.7. Sample D (0.32 A/W at 1.6 V) has the highest responsivity among the three samples. It is expected that sample D has the highest responsivity as it has the most signal compared to other samples as observed from the spectral response and photocurrent density data.

Chopper

Blackbody Source → Cryostat → Current Amplifier → Spectrum Analyzer
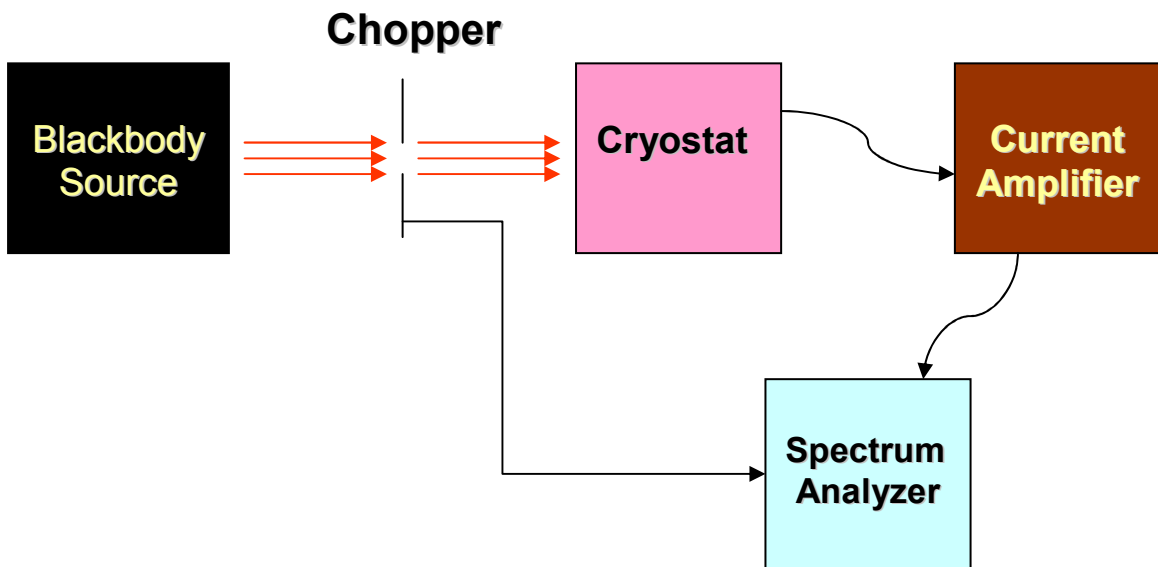
Figure 2.6: Responsivity/Noise measurement setup

The noise from the sample is measured using a 300K scene, which is then amplified by a current preamplifier at each bias and the output from the preamplifier is fed as input to the SRS 550 fast fourier transform (FFT) analyzer. The detectivity (D*) is then deduced from the measured responsivity, detector area (A_d), frequency bandwidth

(Δf) and $i_n / \sqrt{\Delta f}$ is the noise density measured under dark environment as shown in the following equation:

$$D^* = \frac{R_P \sqrt{A_d}}{i_n / \sqrt{\Delta f}} \quad .$$
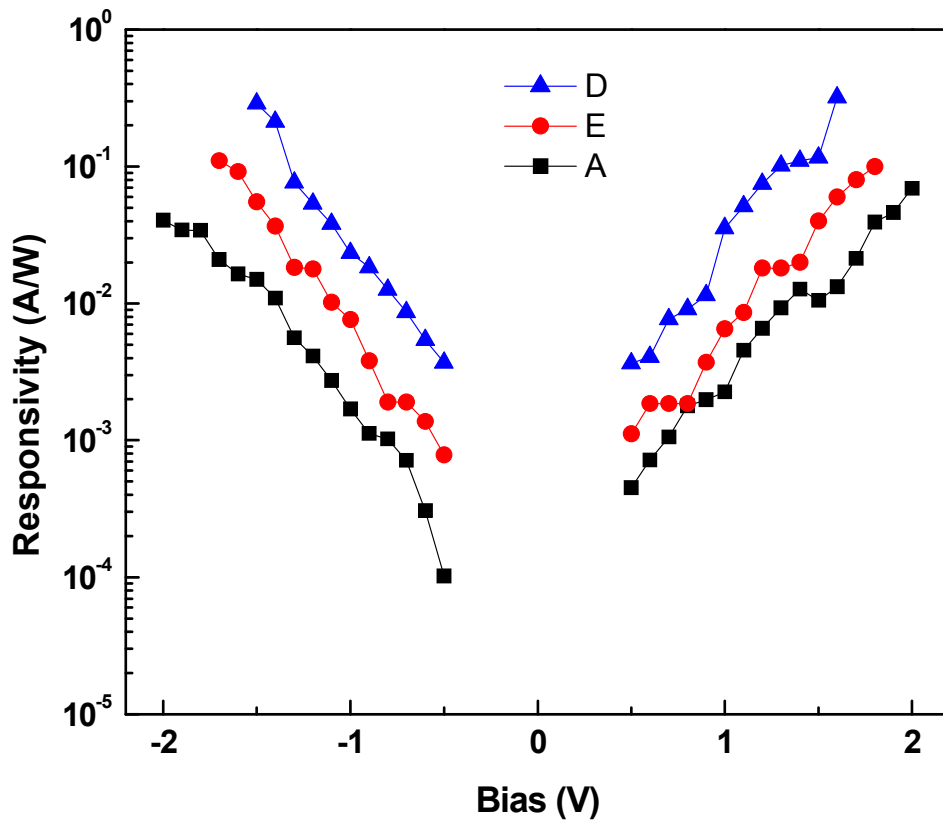
Figure 2.7: Peak responsivity for Samples A(undoped), D(3 x 10^{10} cm^{-2}) and E(6 x 10^{10} cm^{-2}) measured at T=77K.

The measured generation-recombination limited detectivity (D*) is shown in Figure 2.8. The D* data is measured for the samples A, D and E. As observed from the figure sample D has the highest detectivity. This proves that sample D (3×10^{10} cm^{-2}) is the optimal doping for the InAs/In$_{0.15}$Ga$_{0.85}$As DWELL based photodetector. This agrees well with the BLIP data.
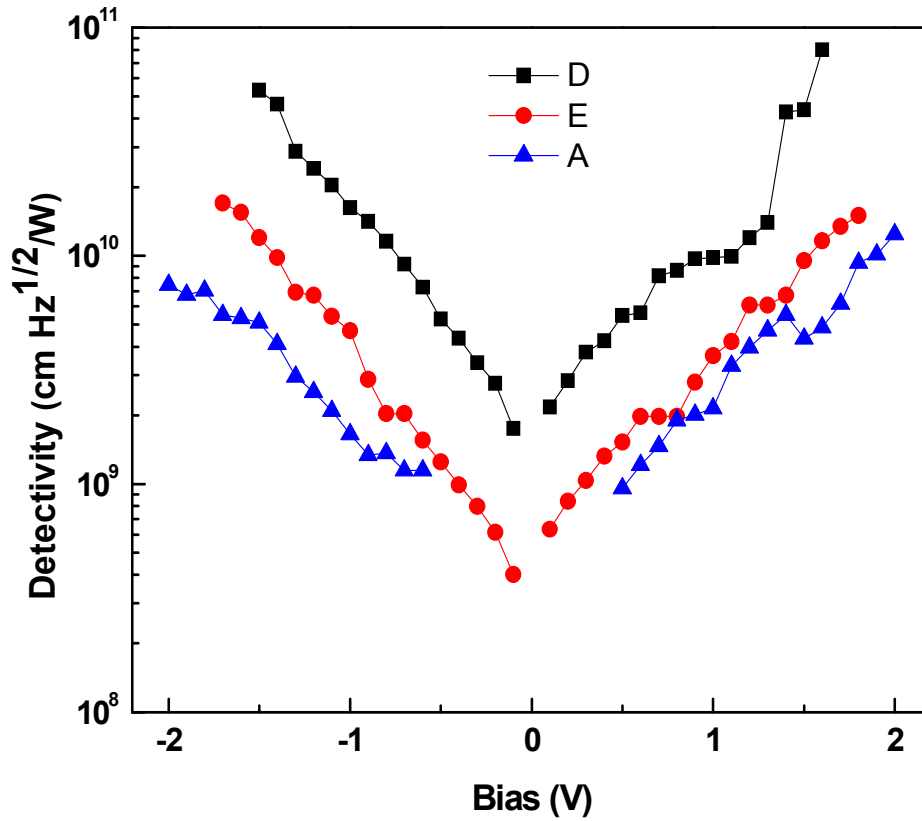
Figure 2.8: Peak Detectivity of samples A, D and E at 77K.

2.5   Conclusion

In summary, the effects of doping on the performance of InAs/In$_{0.15}$Ga$_{0.85}$As dots-in-well (DWELL) infrared photodetectors were determined. An increase in spectral response and dark current density with Si doping is observed. The BLIP which is a

measure of optimal ratio of signal and noise is highest (i.e. 91K) for sample D which has a doping of 3 x 10^{10} cm^{-2}. This is supported by the detectivity (D*) data which is highest (8 x 10^{10} jones at 1.6 V) for sample D. Spectral response and D* reduced for Sample E (6 x 10^{10} cm^{-2}) due to the filling of excited states by additional carriers from the InAs/ In$_{0.15}$Ga$_{0.85}$As layers. However, the dark current density increased by more than 2 orders of magnitude with increase in the doping level. Based on BLIP data and detectivity measurements it can be concluded that 3 x 10^{10} cm^{-2} is the optimal doping for InAs/In$_{0.15}$Ga$_{0.85}$As DWELL photodetectors. The residual doping from the InAs layers may be providing additional carriers, as evidenced by the spectral response obtained from the undoped sample.

1 Mohamed B El Mashade, M Ashry and A Nasr, Semicond. Sci. Tech. 18, 891, (2003).

2 Z Chen et al, J. Appl. Phys., 89(8), 4558, (2001).

3 E T Kim et al, Appl. Phys. Lett. 84, 3277, (2004).

4 S Chakrabarti et al, IEEE Photon. Tech. Lett., 16, 1361, (2004).

5 U H Lee et al, Jpn. J. Appl. Phys., 43, 5199, (2004).

6 R.S. Attaluri et al., J. Appl. Phys., 99, 083105 (2006)

7 R. S. Attaluri et al, J. Vac. Sci. Technol. B, 24(3), May 2006.

8 R.Kaspi and K.R.Evans, Appl. Phys. Lett., 67(6), 819, (1995).

9 O.Brandt, K.Ploog, L.Tapfer, M.Hohenstein, R.Bierwolf and F.Philipp, Phys. Rev. B, 45(15), 8443, (1992).

10 S.Krishna, J. Phys. D: Appl. Phys. 38 (2005) 2142-2150.

11 S. D. Gunapala and K. M. S. V. Bandara, *Thin films*, **21**, p. 113, 1995

Chapter 3

Resonant Cavity Enhanced InAs/In$_{0.15}$Ga$_{0.85}$As DWELL Infrared Detectors

3.1 Introduction

In the previous chapter, investigation of optimal doping for the InAs/In$_{0.15}$Ga$_{0.85}$As dots-in-well (DWELL) QDIP has been performed. The optimal doping is found to be 3 × 10^{10} cm^{-2} and the sample with the optimal doping has the highest responsivity and detectivity. In this chapter, design modification to the QDIP, by incorporating the active region in a resonant cavity is investigated.

QDIPs suffer from low QE due to a low absorption cross-section of the multilayer quantum dot ensemble, relative to the bulk or QW-based detectors [1]. The QE of the QDIPs can be improved by increasing the QD density, the number of QD layers, or by enhancing the absorption of the active region. In typical QDIPs only a single pass of infrared photons is possible on the active region. Photons which are not absorbed in standard QDIPs on the first pass are able to propagate through the active regions, and may not be subsequently absorbed. In our approach, we have designed a new structure where the active region (i.e. DWELL) along with the DBR layers form an asymmetrical resonant cavity (RC-DWELL). The RC enhanced photodetector is formed by placing a thin active region in a fabry-perot cavity cladded with photon reflectors (i.e. DBRs). The fabry-perot cavity is designed in such a way that the optical field for wavelengths near the peak sensitivity of the DWELL detector is enhanced. In our case, the cavity is

cladded with a bottom DBR mirror formed by 2-periods of $Al_xO/GaAs$ (94% reflectivity) and the top mirror is an air/semiconductor interface which provides 30% reflectivity. The fabry-perot cavity traps the light at the resonant wavelength and forces multiple passes of light through the active region enhancing the absorption of the detector, which in turn increases the QE of the device. Resonant cavity enhanced photodetectors with peak QE's of 33-59% have been reported in the literature [2]-[4]. This exemplifies that a resonant cavity enhances the performance of the device and therefore it is a promising technology. Several groups have reported improved performance of detectors due to enhancement provided by the resonant cavity [5]-[10].

3.2 Fabry-Perot Cavity

The Fabry-Perot resonator is an optical cavity with two opposing flat mirrors, which reflect the trapped light multiple times. Due to effects of interference certain wavelengths of light will be reinforced by the cavity, while other wavelengths are suppressed due to destructive interference. Figure 3.1 shows the multiple reflections of the light entering the cavity [11]. Constructive interference occurs when the reflected light which is a combination of many beams are in phase. Similarly, if the many beams of transmitted light are in phase, it corresponds to a high transmission peak of the cavity. Resonance occurs in the cavity when the cavity length is an integral multiple of half the wavelength. Assuming no absorption in the cavity and no relative phase change due to reflections from the mirrors the condition for resonance is given by [12]:

$$m = \frac{\delta}{2\pi} = \frac{2n_s l \cos\theta_s}{\lambda} \quad ,$$

Where n_s is the effective refractive index of the cavity, θ_s is the angle of incidence into the cavity, l is the length of the cavity, δ is the phase difference between each succeeding reflection, λ is the wavelength of the incident light and $m = 0, \pm 1, \pm 2, \ldots$ is the mode of the cavity.
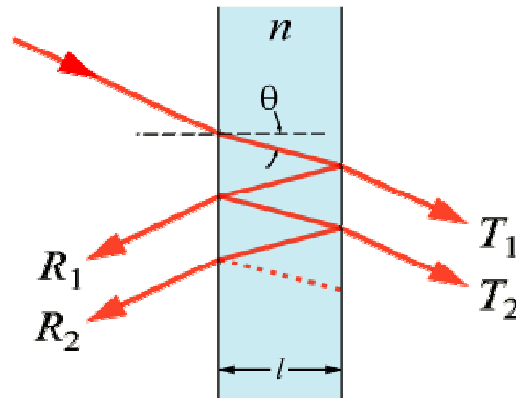
Figure 3.1: Internal reflections in a fabry-perot cavity

3.2.1 Figures of Merit

Most of the figures of merit for fabry-perot cavities describe the spectral width of the cavity. The most important figure of merit for a cavity is Finesse, which is the ratio of the free spectral range (FSR) and the full width half-maximum (FWHM). FSR is the separation between two resonant peaks and the FWHM is the spectral width at 50% of the transmission peak. Generally, the higher the finesse, the narrower the transmission peak and deeper the rejection region [13]. Figure 3.2 illustrates the transmittance of a fabry-perot filter as a function of wavelength [11].
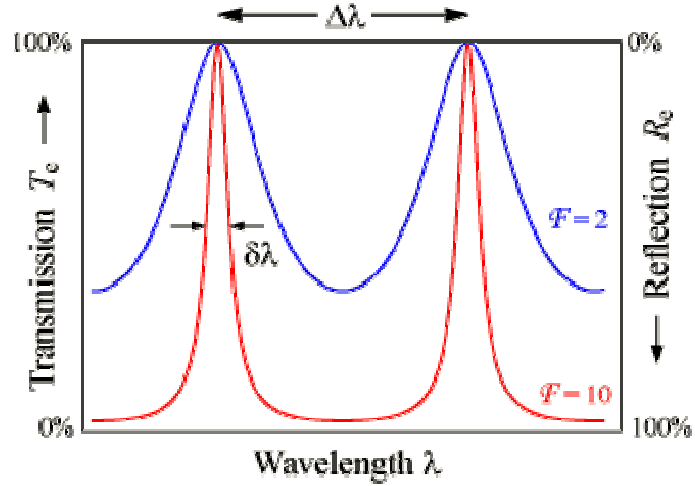
Figure 3.2: Illustration of finesse, FWHM and FSR of a cavity

For matched mirrors the finesse is given by [14]:

$$F = \frac{\pi \sqrt{R}}{1 - R},$$

Where R is the nominal reflectance of both mirrors.

Another important figure of merit for a cavity is the quality factor, Q, which relates the energy within the cavity to the incident energy. A higher Q indicates a narrower spectral line width and is related to the finesse by the resonant frequency, v_o, and the mode spacing, v_F [12]:

$$Q = \frac{v_o}{v_F} F$$

3.2.2   Distributed Bragg Reflector

For resonant cavity enhanced (RCE) semiconductor fabrication, dielectric stack mirrors are used especially for IR wavelengths. The dielectric mirrors consist of alternating high refractive index (n_H) and low refractive index (n_L) dielectric materials. Each layer has a reflectance that is lower than a metal mirror but the total reflectance for

37

the dielectric mirror is a combination of the reflections from all the layers. The total reflectance can approach unity if all the reflections from the layers sum in phase. The simplest layer thickness to achieve in-phase reflections is the equivalent optical thickness of quarter wavelength. This dielectric stack mirror involving alternating high and low refractive index layers is therefore called a quarter-wave-stack (QWS) mirror or distributed bragg reflector (DBR) named after W.H. Bragg and S.L. Bragg, since the reflections interfere constructively when the bragg phase condition is satisfied [15]. The Bragg condition is satisfied when

$$n_L t_L = n_H t_H = \frac{m\lambda_0}{4} \quad m = 1, 3, 5\ldots,$$

where n_H is the index of refraction of the high refractive index dielectric material and n_L is the index of refraction of the low refractive index dielectric material. The thickness of the low and high refractive index materials are t_L and t_H respectively. Also, m is the mode of the cavity and λ_0 is the wavelength.

3.3   Design of Resonant Cavity for DWELL Heterostructure

The resonant cavity is designed for the long wave response at 9.5 μm, which is an important wavelength for mine detection. The structure of the RC-DWELL sample is shown in Figure 3.3. The asymmetric cavity consists of 8-periods of InAs/In$_{0.15}$Ga$_{0.85}$As dots-in-well (DWELL) layers enclosed between a bottom DBR (i.e. 94% reflectivity at 9.5 μm) and air/semiconductor interface acting as top reflector (i.e. 30% reflectivity at 9.5 μm). The bottom DBR consists of two-periods of Al$_x$O/GaAs layers. The design and reflectivity of the DBR is discussed in section 3.3.1.

A control sample with the same active region as the RC-DWELL sample and no bottom DBR is grown along with the RC-DWELL sample in order to compare the performance of the resonant cavity based structure with the regular DWELL sample. The heterostructure schematic of the standard 8-periods of $InAs/In_{0.15}Ga_{0.85}As$ DWELL sample is shown in Figure 3.4. The details of the crystal growth of the RC-DWELL and the standard DWELL samples are discussed in section 3.4. Figure 3.5 shows the simulated electric field of the 9.5 μm light wave with respect to distance into the RC-DWELL cavity. A closer look reveals the overlap of the maxima of the electric field with the DWELL layers which increases the absorption of the light by the QDs.

The simulated and experimental reflectivity spectrums of the RC-DWELL are shown in Figure 3.6. From the figure a dip in reflectivity at 9.5 μm is observed for both experimental and simulated spectrums which show the resonant wavelength for the cavity. The difference between the experimental and simulated reflectivity spectrums specifically in the 10–16 μm range can be attributed to the shrinkage of the $Al_{0.98}Ga_{0.02}As$ layers after oxidation which might have altered the periodic change in refractive indices. Some peeling of layers was also observed after the oxidation process of the entire cavity. The oxidation process is described in detail in section 3.5.1 of this chapter.
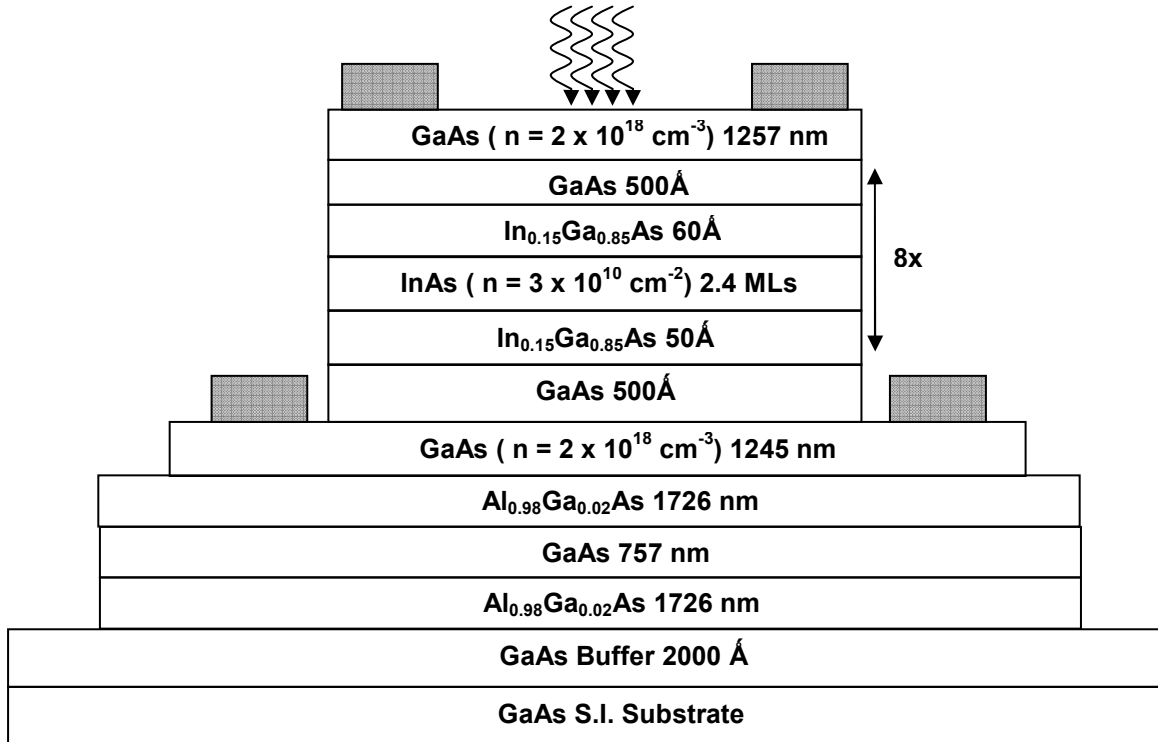
Figure 3.3: Heterostructure schematic of a Resonant Cavity (RC) 8-period

InAs/In$_{0.15}$Ga$_{0.85}$As DWELL infrared photodetector
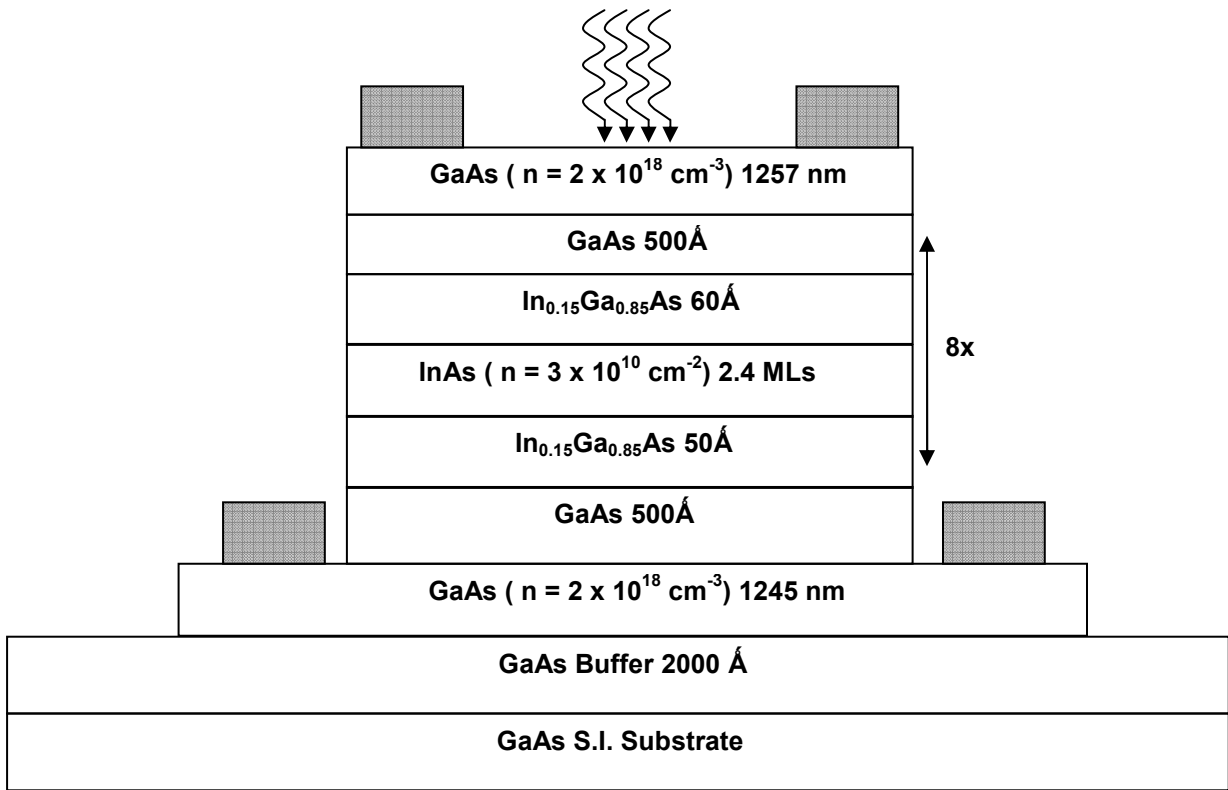
Figure 3.4: Heterostructure schematic of a 8-period InAs/In$_{0.15}$Ga$_{0.85}$As DWELL infrared photodetector

The diagram shows a layered heterostructure (top to bottom):

- GaAs (n = 2 x 10^{18} cm^{-3}) 1257 nm
- GaAs 500Å
- In$_{0.15}$Ga$_{0.85}$As 60Å
- InAs (n = 3 x 10^{10} cm^{-2}) 2.4 MLs
- In$_{0.15}$Ga$_{0.85}$As 50Å
- (8x for the layers from GaAs 500Å through In$_{0.15}$Ga$_{0.85}$As 50Å)
- GaAs 500Å
- GaAs (n = 2 x 10^{18} cm^{-3}) 1245 nm
- GaAs Buffer 2000 Å
- GaAs S.I. Substrate
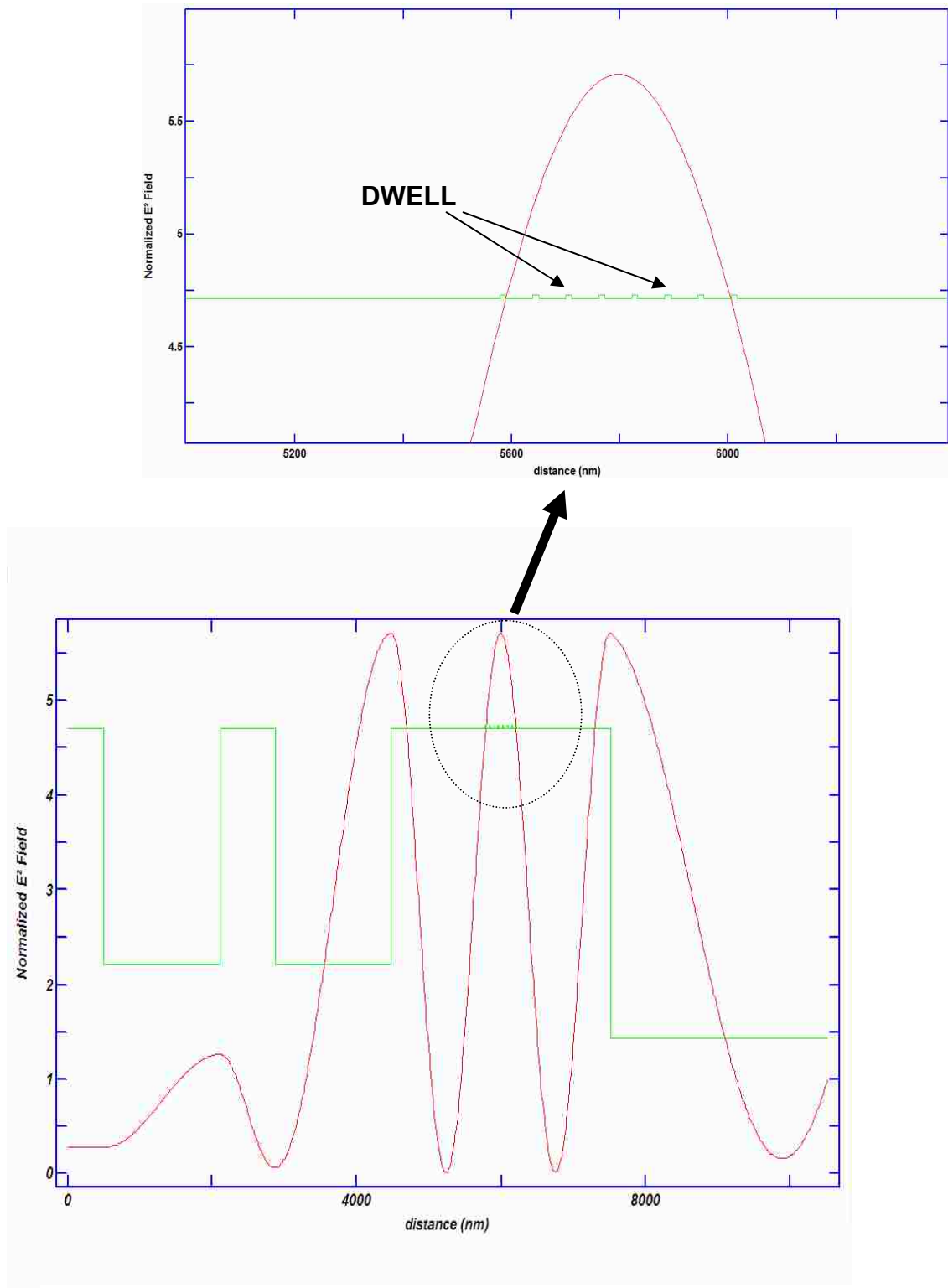
Figure 3.5: Plot of Normalized Squared Electric field versus the distance into the cavity
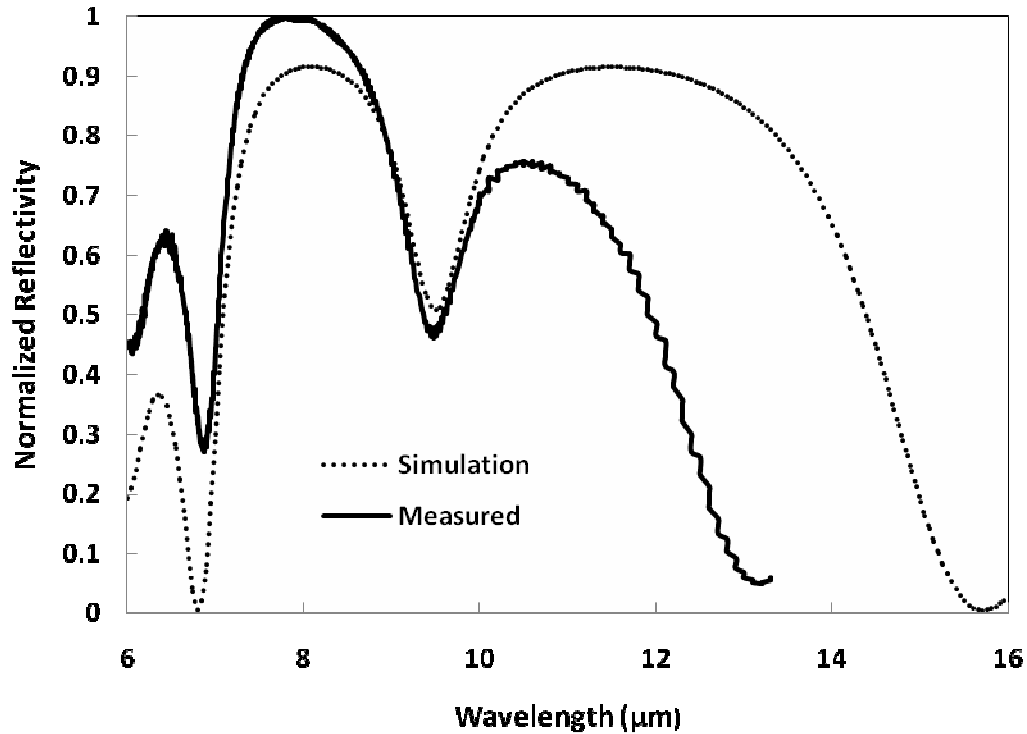
Figure 3.6: Simulated and experimental reflectivity of the RC-DWELL cavity

3.3.1 Design of Distributed Bragg reflector (DBR)

The distributed bragg reflector for the current work is based on AlO_x/GaAs materials. The advantage of this structure over that of AlAs/GaAs based mirrors is the low refractive index of AlO_x and the thickness required for the mirrors to obtain decent reflectivity is low. The bottom DBR consists of 2-periods of $Al_{0.98}Ga_{0.02}As$ /GaAs, where the $Al_{0.98}Ga_{0.02}As$ layers are oxidized to form Al-based oxide with a refractive index of 1.55. The design of the bottom DBR is shown in Figure 3.7. The $Al_{0.98}Ga_{0.02}As$ layer is grown as a 1 monolayer GaAs/49 monolayers AlAs digital alloy. The growth of the bottom DBR is discussed in detail in Section 3.4. The simulated and experimental reflectivity spectrums are shown in Figure 3.8. The DBR mirror has a broad reflectivity

spectrum and has 94% reflectivity at 9.5 μm. The reflectivity of the DBR was measured using a standard reflection accessory in a Nicolet 6700 FTIR. The background reflectivity spectrum was measured using a gold mirror and then the actual sample was measured. One thing to note about the setup is that light is incident at an angle closer to 90°.

Without the oxidation process, 9-periods of 829nm $Al_{0.98}Ga_{0.02}As$/ 719 nm GaAs are required in order to obtain 90% reflectivity around 9.5 μm. The oxidation process results in formation of Al-based oxide that has a low refractive index of 1.55, thereby reducing the number of periods required to obtain 90% or more reflectivity at 9.5 μm.
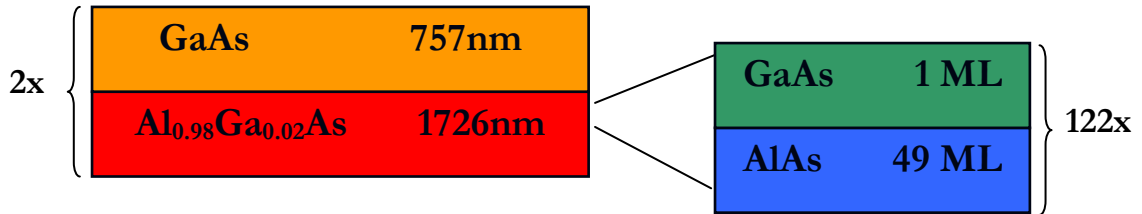
Figure 3.7: Schematic of the bottom DBR
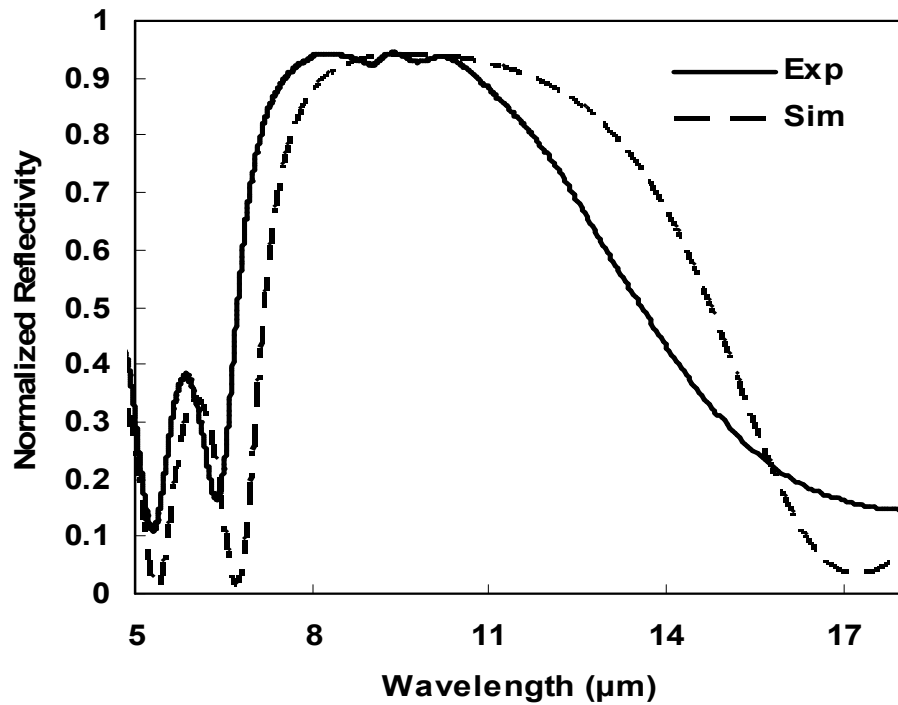
Figure 3.8: Simulated and experimental reflectivity spectrums of the bottom distributed bragg reflector (DBR)

3.4 Growth

Two samples with resonant cavity (RC-DWELL) and standard DWELL were grown in a VG Semicon V80H MBE (Molecular Beam Epitaxy) reactor. The structures of the RC-DWELL and the standard DWELL samples are shown in Figures 3.3 and 3.4. The RC-DWELL sample was grown with an 8-stack DWELL active region consisting of 2.4 MLs of InAs QDs in 110 Å $In_{0.15}Ga_{0.85}As$ QW separated by 500 Å GaAs barriers. The growth of the DWELL layers is described in detail in chapter 2. The resonant cavity (T_c=9.5 μm) was formed with a DBR beneath the DWELL n-i-n detector structure and semiconductor-air interface above the detector structure. The DBR consists of two periods of 757 nm GaAs and 1726 nm $Al_{0.98}Ga_{0.02}As$ quarter wave pairs. In the second

period of the DBR, after the growth of the $Al_{0.98}Ga_{0.02}As$ layer, the GaAs layer is combined with the bottom GaAs contact layer. The reason for combining the GaAs DBR layer with the bottom contact is to increase the thickness of the contact layer which will ensure the availability of enough free carriers through the device. In addition, it will help overcome any problems related to fabrication of the device like variation of etch rate for dry etching of the mesa. The DBR structure was grown at $560^{o}C$; $Al_{0.98}Ga_{0.02}As$ layers were grown as 122-periods of 1 ML (2.83 Å) GaAs/49 MLs (~139 Å) AlAs digital alloy. For the growth of the $Al_{0.98}Ga_{0.02}As$ and the GaAs layers, the growth rates of Ga and Al cells were set to 0.75 ML/s. The growth rates for the cells were calibrated using RHEED and XRD.

3.5   Device Fabrication

Device fabrication is done in a class-100 cleanroom where 380 μm x 380 μm mesas were defined using photolithography, metal evaporation and dry etching techniques. Figures 3.9, 3.10 and 3.11 show the masks used for the RC-DWELL sample. The processing of the photodetector consisted of three steps as shown in Figure 4.3. In the first step, the mesa is defined using photolithography followed by an ICP etch. In the second step, the top and metal contacts are defined using photolithography, followed by metal deposition and metal liftoff. The final step consists of photolithography and dry etch to the bottom DBR. After the final etch to the DBR, the top and bottom contacts are annealed under a N_2 rich atmosphere. The bottom DBR is laterally oxidized in a steam oxidation furnace at

a temperature of 435° C for 90 minutes. The oxidation process is described in the next section.
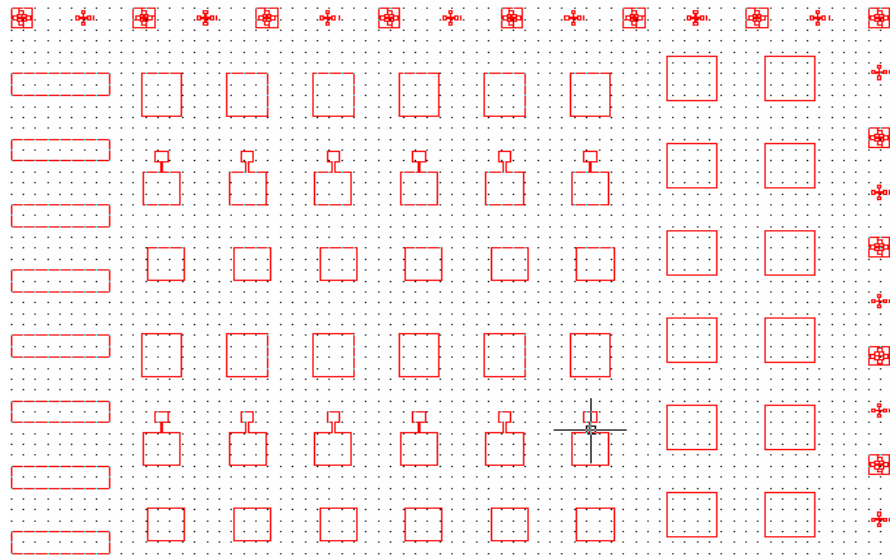
Figure 3.9: Autocad image of mask for mesa etch
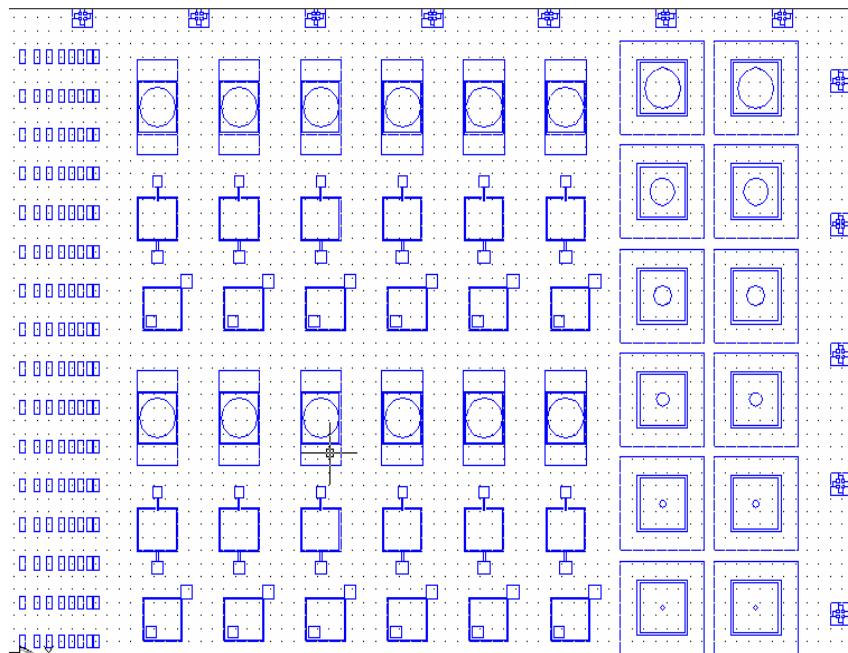
Figure 3.10: Autocad image of mask for top and bottom metal deposition
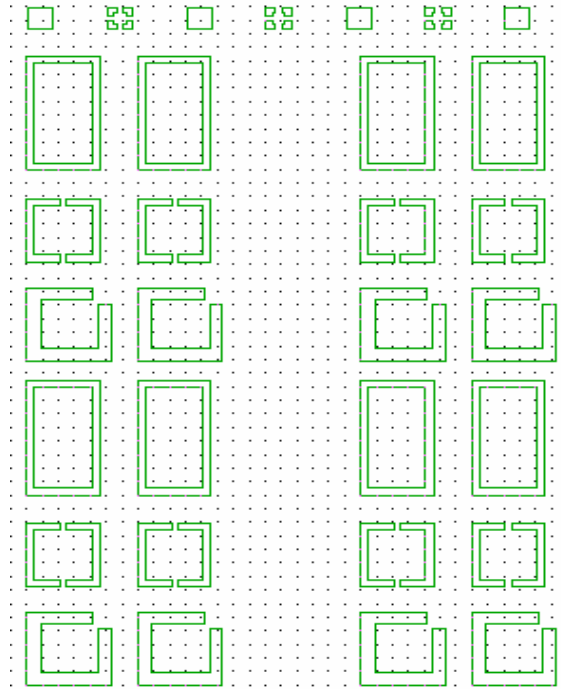
Figure 3.11: Autocad Image of mask for bottom DBR etch

Mesa etching

Top & bottom contact
metal deposition

Bottom DBR etching
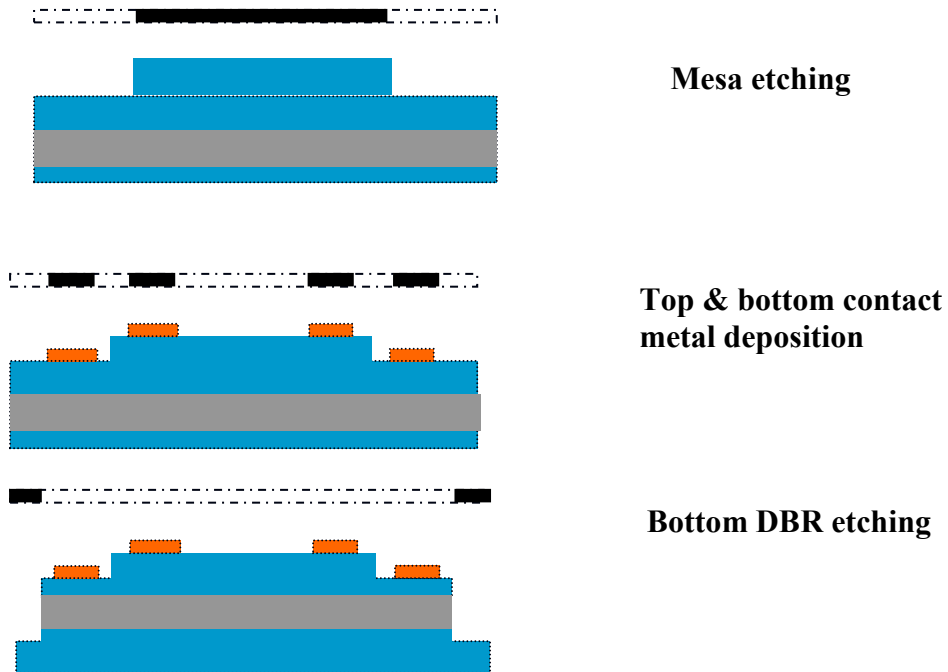
Figure 3.12: Fabrication process of RC-DWELL sample

3.5.1 Oxidation

The oxidation setup consists of a tube furnace through which hot water vapor is carried by a carrier gas N_2. The furnace and the water bath are temperature controlled to ensure repeatability and consistency of the process. If lateral oxidation is desired, mesas of the material must be etched such that sidewalls of layers to be oxidized must be exposed. Figure 3.13 illustrates the oxidation furnace and the chemical reaction consistent with the formation of the steam oxide [16].
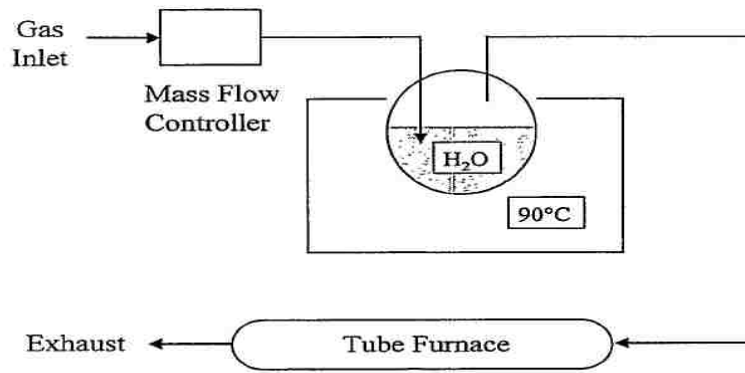
Figure 1. Oxidation apparatus

Figure 3.13: Illustration of steam oxidation furnace and the chemical

equations behind the oxidation process

The term ΔG^{698} in the figure refers to the gibbs free-energy at a temperature of 698K. It should be noted that the chemical equations listed in the figure have negative free-energy, which implies that the process is exothermic. It can be observed that the reactions include

the intermediate formation of AsH_3 and Arsenic (i.e. As). Raman studies have indicated a relatively constant As flow during the oxidation process which implies that there is a balance in between the chemical reaction to loss of As and formation of As. The mechanism for removal of As from the oxide is not strong enough to remove all of the As, since elemental As is found in or around the oxidized regions. Transmission electron microscope (TEM) studies show that the oxide formed is a γ-phase Al_2O_3. If the AlAs is replaced by GaAs in equation [1], this results in a positive gibbs free-energy $\Delta G^{698} = + 10$ KJ/mol making it thermodynamically unfavorable. Therefore, adding even a minute amount of Ga to AlAs results in greatly slows down the oxidation rate. Figure 3.14 shows the oxidation rate of AlGaAs as a function of Al mole fraction [16].
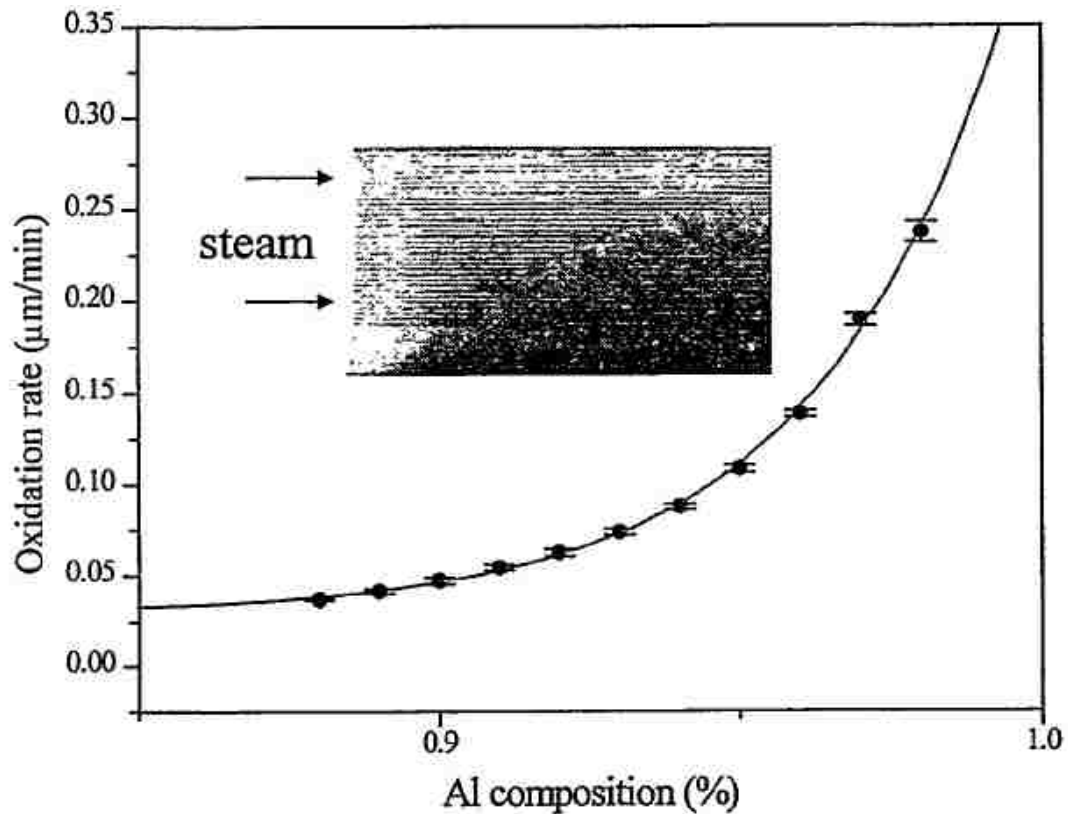
Figure 3.14: Oxidation rate of AlGaAs as a function of Al mole fraction

From Figure 3.14 and the positive gibbs free-energy it can be concluded that the oxidation rate of GaAs based layers is negligible compared to the oxidation rate of $Al_{0.98}Ga_{0.02}As$. Therefore, the oxidation process does not affect the active region (i.e. $InAs/In_{0.15}Ga_{0.85}As$ DWELLs) significantly and the leakage current may be negligible.

After processing detector mesas, the $Al_{0.98}Ga_{0.02}As$ layers were oxidized at 435° C in an N_2/H_2O vapor environment for 75-90 minutes, which decreased the refractive index to 1.55. The oxidation rate is calibrated with a sample that has just the DBR structure and then the actual sample is oxidized based on the oxidation rate. It has been shown that oxides formed from AlGaAs are superior to AlAs in terms of oxidation isotropy, mechanical stability and lack of strain. In addition, they are electrically insulating and have low refractive index. They have been shown to dramatically improve the performance of near IR VSCELs [17] [18]. The reflectivity of the DBR at 9.5 μm was 94% based on simulation and experimental results as shown in Figure 3.8. The DBR exhibited a wide reflectivity range (i.e. 8-12 μm) which is desirable for long wavelength response from the photodetector.

3.6   Device Characterization

The normalized spectral response of the devices, performed with a Nicolet 8700 FTIR-spectrometer, are shown in Figure 3.15. As shown in Fig. 3.15, the long wavelength infrared (LWIR) peak response of the RC-DWELL sample was ~9.5 μm; the resonant wavelength of the optical cavity. The peak LWIR response of the standard DWELL sample was around 10 μm. We note that the LWIR peak is enhanced in comparison to the mid-wavelength infrared (MWIR) 5-7 μm peak, consistent with the

intended effect of the 9.5 μm resonant optical cavity. In the standard DWELL, the similar

widths and intensities of the 6 μm and 10 μm can be attributed to the inhomogeneity of

InAs dots and various transitions between the energy levels of the QD and QW.
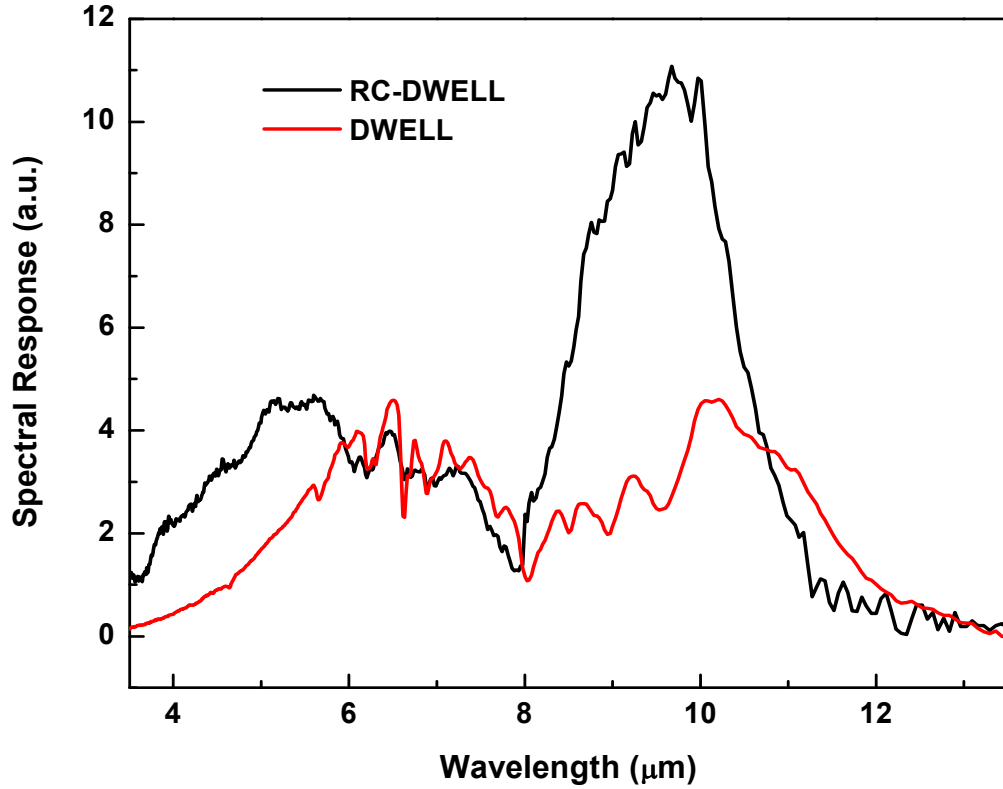
Figure 3.15: Normalized spectral response data for the RC-DWELL and the standard DWELL samples. All the spectra were taken at *T*=30 K at a bias of *V_b*= -1.8V

Fig. 3.16 shows the measured photocurrent when the devices were illuminated by

a 300 K scene under F1.7 conditions. The inset to Fig. 3.16 shows the experimental setup

for the photocurrent measurement. As seen from Fig. 3.16, the RC-DWELL detector

evidenced a higher photocurrent density than the standard DWELL detector. With a 2.1

V bias across the detector at 80K, the photocurrent density increased by a factor of 6 in the RC-DWELL detector as compared to the control sample. The difference in photocurrent density between the normal DWELL and RC-DWELL is negligible below 1.5V due to the dominance of mid wave infrared absorption. The photocurrent density above 1.5V increases drastically as the long wave infrared transition dominates in that bias regime. The resonant cavity has been designed for the long wave response.
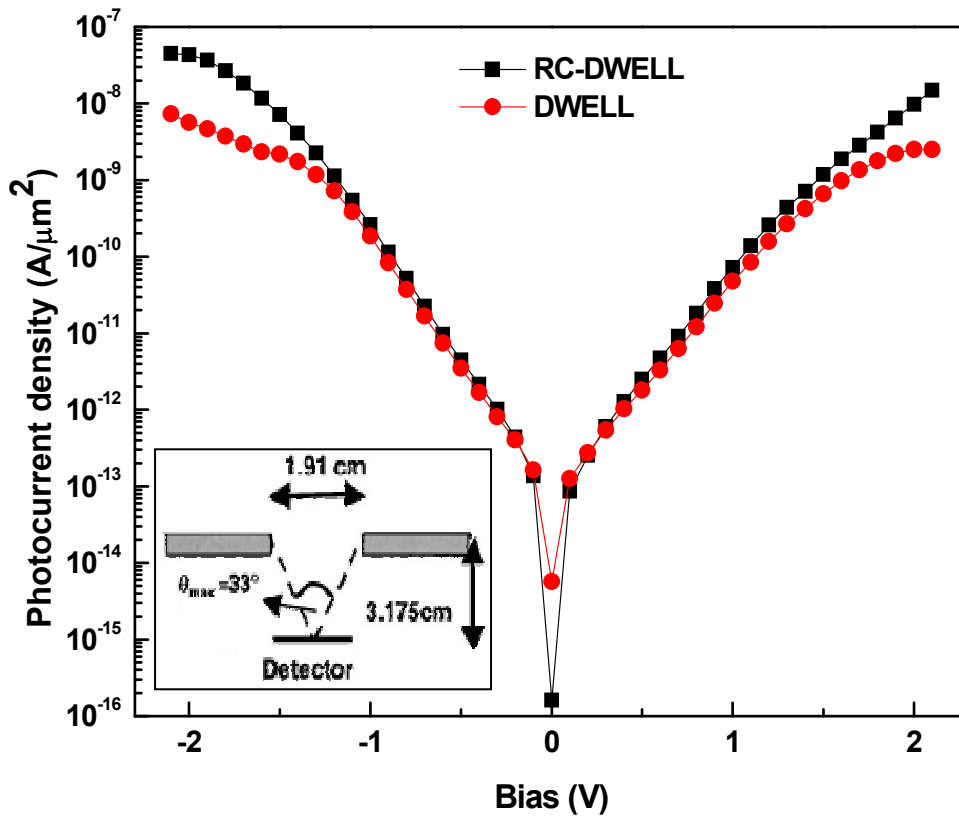
Figure 3.16: A comparison of photocurrent densities for RC-DWELL and the standard DWELL samples at T=80 K obtained with the detector viewing a 300K optical cloth under F1.7 conditions, as shown in the inset

Dark current measurements were performed on the RC-DWELL and the standard DWELL detectors. As shown in Fig. 3.17, the RC-DWELL and the standard DWELL

have comparable dark current density. It is expected that the RC-DWELL sample and the standard DWELL sample have the same current density as they have similar active region and the DBR layers should not affect the dark current density in any way.
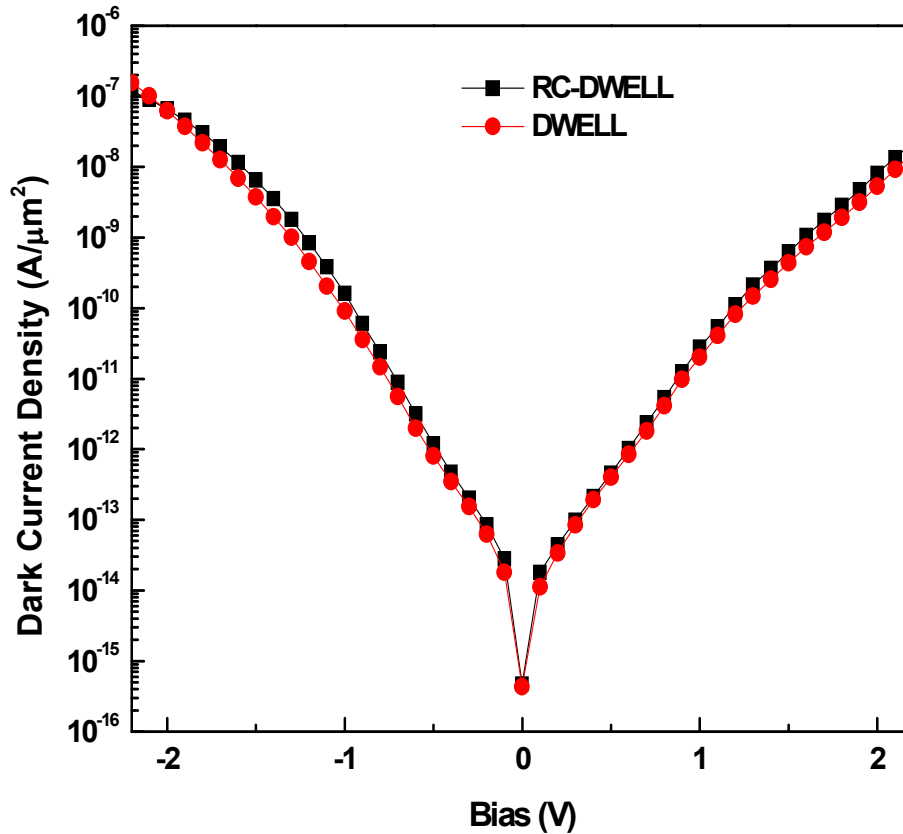
Figure 3.17: Bias dependent dark current densities for RC-DWELL and the standard DWELL samples at *T*=70 K

Calibrated radiometry measurements were undertaken using an 800 K blackbody and an optical chopper to determine the responsivity of the detectors. The responsivity of the RC-DWELL sample was found to be higher than the standard DWELL sample as shown in Fig. 3.18. The highest peak responsivity for the RC-DWELL sample is found to be 0.76 A/W at 1.4 V applied bias and 77K. The responsivity increased by a factor of six as compared to the maximum response of the standard DWELL at 1.2V applied bias. The
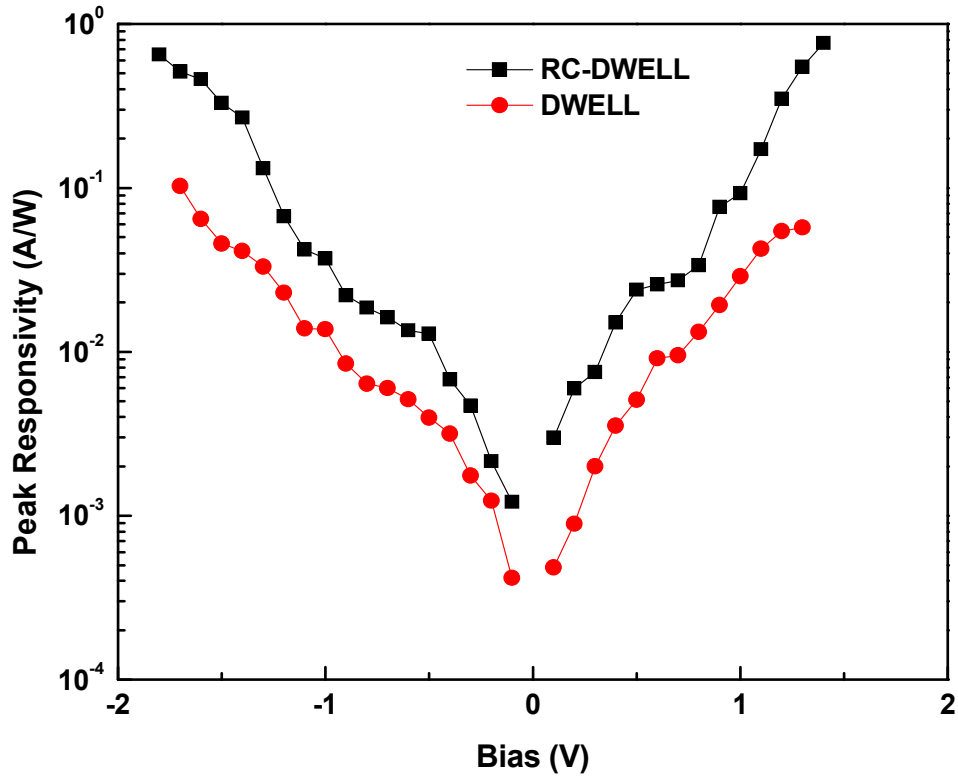
Figure 3.18: Bias dependent peak responsivity for RC-DWELL and the standard DWELL samples at *T*=77 K using a calibrated black body at 800K

increase in responsivity can be inferred from the increase in QE due to the effect of resonant cavity. The QE for the RC-DWELL was found to be 10% at 9.5 μm as compared to the standard DWELL sample, which had a QE of 1.25% at 10 μm. Figure 3.19 shows the generation-recombination limited detectivity (D*) for the RC-DWELL and standard DWELL photodetectors. The detectivity was calculated from the following formula,

$$D^* = \frac{R_P \sqrt{A}}{i_n / \sqrt{\Delta f}},$$

where R is the measured peak responsivity and A is the area of the detector. i_n is the generation-recombination noise current calculated from the total current.

$i_n = 2\sqrt{G*i*q*\Delta f}$, where G is the photoconductive gain, i is the total current and Δf is the detector bandwidth. The photoconductive gain is determined from a control sample for different applied bias.
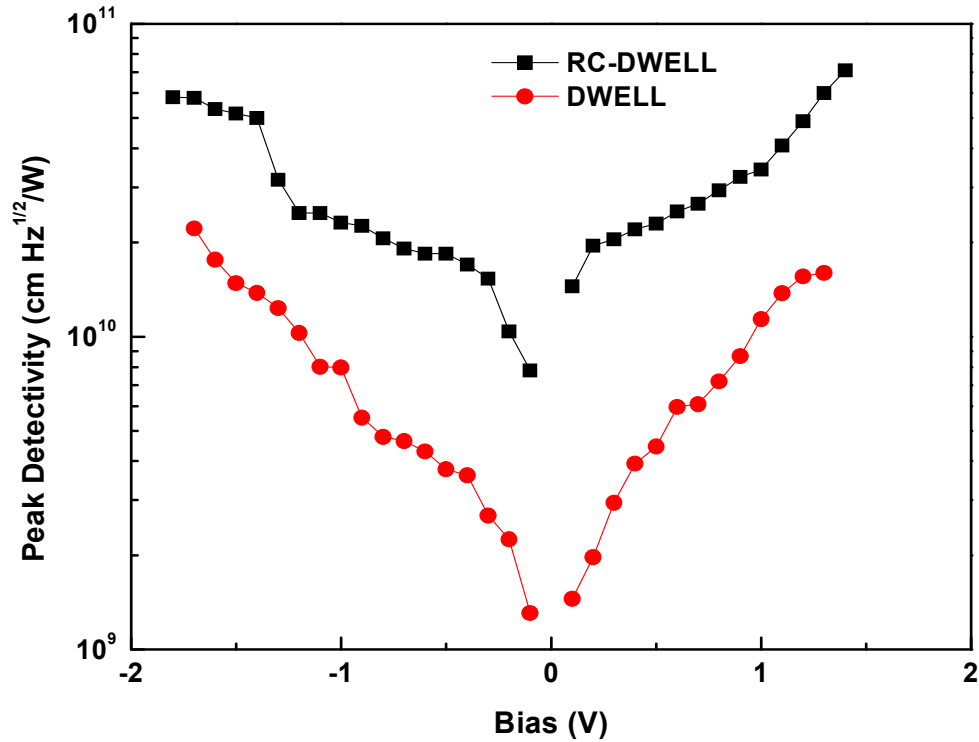
Figure 3.19: Bias dependent peak detectivity for RC-DWELL and the standard DWELL samples at T=77 K while observing a 300K background scene (f 1.7)

The D*, which is a normalized measure of the signal to noise ratio of the detector, was highest (i.e. 1.4 x 10^{10} cm Hz$^{1/2}$/W at a bias of 0.5 V and 77K) for the RC-DWELL. The detectivity of the standard DWELL photodetectors was 9.3 x 10^8 cm Hz$^{1/2}$/W at a bias of 1.2 V and 77K in comparison to the RC-DWELL photodetectors which was 3 x

10^9 cm $Hz^{1/2}$/W at the same bias and temperature. The detectivity increased in comparison to the standard DWELL by a factor of three at a bias of 1.2 V. This result indicates that the resonant cavity significantly improved the performance of the detector.

3.7 Conclusion and Summary

In summary, we have demonstrated a resonant cavity enhanced InAs/$In_{0.15}$ $Ga_{0.85}As$ quantum dots-in-well (RC-DWELL) photodetector. We have experimentally compared the RC-DWELL to a standard DWELL detector. We have observed an increase in the photocurrent density by a factor of 6 at 2.1V and 80K relative to the standard DWELL detector. We measured corresponding increases in the responsivity and detectivity of the RC-DWELL detector in comparison to the standard DWELL detector. The peak responsivity of the RC-DWELL detector was 0.76 A/W at 1.4V applied bias and the peak detectivity was 1.4 x 10^{10} cm $Hz^{1/2}$/W. We conclude that the resoant cavity has significantly enhanced the performance of the DWELL detector due to the increase in the QE of the device.

[1] S. D. Gunapala, S. V. Bandara, C. J. Hill, D. Z. Ting, J. K. Liu, S. B. Rafol, E. R. Blazejewski, J. M. Mumolo, S. A. Keo, S. Krishna, Y. C. Chang, and C. A. Shott, Proc. SPIE Vol. 6206, 62060J (2006).

[2] Q. Han, X. H. Yang, Z. C. Niu, H. Q. Ni, Y. Q. Xu, S. Y. Zhang, Y. Du, L. H. Peng, H. Zhao, C. Z. Tong, R. H. Wu, and Q. M. Wang, Appl. Phys. Letters, 87, 111105 (2005).

[3] Hui Huang, Yongqing Huang, Xingyan Wang, Qi Wang, and Xiaomin Ren, IEEE Photonics Tech. Lett., 16(1), 2004.

[4] R. W. Mao, Y. H. Zuo, C. B. Li, B. W. Cheng, X. G. Teng, L. P. Luo, J. Z. Yu, and Q. M.Wang, Appl. Phys. Lett., 86, 033502 (2005).

[5] M.S. Unlu, K. Kishino, J.I. Chyi, L. Arsenaul, J. Reed, S. Noor Mohammad, and H. Morkoc, Appl. Phys. Lett., 57(8), 750, (1990).

[6] C. Lenox, H. Nie, P. Yuan, G. Kinsey, A. L. Holmes Jr., B. G. Streetman, and J. C. Campbell, IEEE Photon. Tech. Lett., 11(9), 1162, (1999).

[7] J.D. Schaub, R. Li, C. L. Schow, J. C. Campbell, G. W. Neudeck, and J. Denton, IEEE Photon. Tech. Lett., 11(12), 1647, (1999).

[8] J. G. A. Wehner, C. A. Musca, R. H. Sewell, J. M. Dell, L. Faraone, Appl. Phys. Lett., 87, 211104, (2005).

[9] J. L. Pautrat, E. Hadji, J. Bleuse, and N. Magnea, J. Elec. Mat., 26(6), 667, (1997).

[10] M. Arnold, D. Zimin, and H. Zogg, Appl. Phys. Lett., 87(14), (2005).

[11] http://en.wikipedia.org/wiki/Fabry-Perot

[12] Justin G. A. Wehner. Investigation of Resonant-cavity-enhanced mercury cadmium telluride infrared photodetectors. Dissertation, University of Western Australia.

[13] G. Hernandez. Fabry-perot interferometers. Cambridge University press, Cambridge, 1988.

[14] Max Born and Emil Wolf. Principles of optics: electromagnetic theory of propagation, interference and diffraction of light. Cambridge university press, Cambridge, 1999.

[15] R. Riley. Bragg's Law for X-ray Crystal Diffraction. Phys. Educ., 5:371-372, 1970.

[16] Olga B. Spahn, Andrew A. Allerman, Kent D. Choquette, Gregory A. Vawter, John F. Klein, Charles T. Sullivan, John P. Sullivan, Carol I.Ashby, Arlee V. Smith, Thomas D. Raymond and William J. Alford, Sandia Report, SAND99-0921, Sandia National Laboratories, July 1999.

[17] Kent D. Choquette, K. M. Geib, H. C. Chui, B. E. Hammons, H. Q. Hou, T. J. Drummond and Robert Hull, Appl. Phys. Lett., 69 (10), 1996.

[18] P. C. Ku, Jacob A. Hernandez, and C. J. Chang-Hasnain, IEEE Photonics Tech. Lett., 15(1), 2003.

Chapter 4

Growth and Performance of InAs/In$_{0.15}$Ga$_{0.85}$As/GaAs DWELL Infrared Photodetector

4.1 Introduction

In Chapter 3, investigation of resonant cavity enhanced InAs/In$_{0.15}$Ga$_{0.85}$As DWELL-based detector has been undertaken. Photoresponse at the cavity resonance (T$_c$ = 9.5 µm) has been measured. A significant increase in QE, responsivity (i.e. factor of six) and detectivity (i.e. factor of three) has been observed. In this chapter, design modification to the DWELL to increase the QE is investigated.
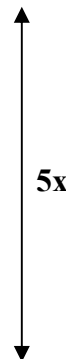
Infrared photodetectors with an InAs/In$_{0.15}$Ga$_{0.85}$As DWELL active region suffer from strain related issues. Due to high compressive strain, a greater number of active region layers cannot be grown without introducing dislocations. More layers translate into increased absorption, which in turn increases the QE of the photodetector. This increase in QE will increase the responsivity and detectivity of the detectors.

In our group, we have been investigating alternate heterostructures based on DWELL active region which have low strain to incorporate greater number of DWELL layers into the active region. The goal is to increase the QE and operating temperature of the DWELL design. We have designed an alternative structure with low strain and similar conduction band offset to the standard InAs/In$_{0.15}$Ga$_{0.85}$As DWELL structure discussed in the introduction and the previous chapters. The new DWELL structure has InAs QDs embedded in a double well structure consisting of In$_{0.15}$Ga$_{0.85}$As QW in a

GaAs QW, which in turn is surrounded by $Al_{0.1}Ga_{0.9}As$ barriers. Based on the thickness of the QW and QD layers, the average indium composition in this new DWELL design is 5% and that corresponds to 0.35% compressive strain. The average indium composition in the standard DWELL is about 19%, which corresponds to 1.35% compressive strain on GaAs. Compared to the standard DWELL design the new DWELL design has very low strain and therefore greater number of DWELL layers can be grown without introducing any dislocations. A 30-period sample based on this new design has been grown, fabricated and characterized. Preliminary results from a 30-period device structure yielded good performance. This alternative DWELL structure shows promise and needs to be investigated more in the future.

4.2 Growth

Initially, a number of calibration structures were grown to obtain an optimal design for the new DWELL structure. Figure 4.1 and table 4.1 show the calibration structures grown and the key differences between them. Room temperature PL measurements were used to characterize the material and optical quality of the DWELL layers as described in table 4.1. From the PL measurements it can be concluded that sample #2298 has the best intensity. A 30-stack QDIP based on sample #2298 has been grown. Figure 4.2 shows the heterostructure schematic of the QDIP based on the new DWELL design. The InAs/$In_{0.15}Ga_{0.85}As$/GaAs dots-in-well (DWELL) structure is grown in a VG Semicon V-80H molecular beam epitaxy. The active region consists of 30 periods of DWELL layers separated by 500 Å thick $Al_{0.1}Ga_{0.9}As$ barriers. The DWELL layers consist of 2 MLs of InAs QDs in a 20 Å $In_{0.15}Ga_{0.85}As$ QW which in turn is surrounded by GaAs QW.

Al$_{0.1}$Ga$_{0.9}$As barrier	50nm
GaAs QW	6.85nm
In$_{0.15}$Ga$_{0.85}$As QW	0 - 2nm
InAs QDs	2 MLs
In$_{0.15}$Ga$_{0.85}$As QW	1nm
GaAs QW	0 - 4nm
Al$_{0.1}$Ga$_{0.9}$As barrier	50nm
GaAs buffer	2000nm
GaAs Semi-Insulating Substrate	

5x

Figure 4.1: Calibration structure for low strain alternative DWELL. Highlighted layers show possible variations in the structure. Some of the variations that have been tried are described in Table 4.1.

Sample no.	In$_{0.15}$Ga$_{0.85}$As QW Cap thickness	GaAs first part of QW thickness	PL Wavelength	Intensity [a.u.]
Run 2291	0 nm	0 nm	1054 nm	0.0009
Run 2292	1 nm	0 nm	1080 nm	0.0025
Run 2293	2 nm	0 nm	1079 nm	0.003
Run 2294	1 nm	1nm	1065 nm	0.002
Run 2295	1 nm	2nm	1055 nm	0.007
Run 2296	1 nm	3nm	1060 nm	0.22
Run 2298	1 nm	4nm	1060 nm	0.31

Table 4.1: PL response of Calibration structures for optimizing the DWELL design

The first step in the growth is oxide desorption from the semi-insulating GaAs substrate. The oxide is desorbed at a temperature of 650º C for 10 minutes and then the equivalent thermocouple temperatures for various temperatures required for the growth of different layers are measured. After measuring the equivalent thermocouple temperatures, a 2000 Å thick GaAs buffer layer is grown to smooth the surface and cover any pits formed after oxide desorption. All temperatures during MBE growth are calibrated via a pyrometer. After the buffer layer is grown a 300 Å AlAs etch stop layer is grown, the purpose of this layer is for substrate removal during fabrication process of focal plane array (FPA). A 2 μm thick n+-GaAs bottom contact layer doped with Si at a doping concentration of 2 x 10^{18} cm^{-3} is grown after the AlAs etch stop layer. After the GaAs bottom contact layer, a 500 Å thick $Al_{0.1}Ga_{0.9}As$ barrier is grown at a temperature of 590º C. The buffer, etch stop, and the bottom contact layers are grown at the same temperature. After the $Al_{0.1}Ga_{0.9}As$ barrier is grown, a 300 sec growth interrupt is started to lower the substrate temperature from 590º C to 470ºC for the DWELL layers to be grown. At the end of interrupt, the first part of GaAs QW, which is 40 Å thick, is grown. After the 40 Å GaAs QW, a 0.716 ML InAs seeding layer is grown. In has low sticking coefficient and, when introduced on the surface, it floats and therefore a seeding layer is introduced to prevent a compositional gradient for the $In_{0.15}Ga_{0.85}As$ QW. The thickness of this InAs pre-adsorbed layer varies depending on the thickness of the QW and growth temperature [1]. This InAs seeding layer gets segregated to the top surface and will be evaporated after deposition of a thin enough GaAs layer. After the InAs floating layer is put down on the substrate, a 10 Å thick $In_{0.15}Ga_{0.85}As$ layer, which is the first part of the $In_{0.15}Ga_{0.85}As$ QW, is grown. It has been shown that InAs QDs grown on an $In_{0.15}Ga_{0.85}As$

layer have higher density compared to QDs grown on GaAs [2,3]. Immediately after the growth of the $In_{0.15}Ga_{0.85}As$ layer 1.08 MLs of InAs wetting layer is grown following which 0.2 MLs of additional InAs layer is deposited which form the quantum dots.

GaAs (n = 2 x 10^{18} cm^{-3}) 0.2 μm
$Al_{0.1}Ga_{0.9}As$ 500 Å
GaAs 68.5 Å
$In_{0.15}Ga_{0.85}As$ 10 Å
InAs QDs (n = 1.4 x 10^{11} cm^{-2}) 2 MLs
$In_{0.15}Ga_{0.85}As$ 10 Å
GaAs 40 Å
$Al_{0.1}Ga_{0.9}As$ 500 Å
GaAs (n = 2 x 10^{18} cm^{-3}) 2 μm
AlAs 30 nm
GaAs buffer 0.2 μm
GaAs S.I. Substrate

30x
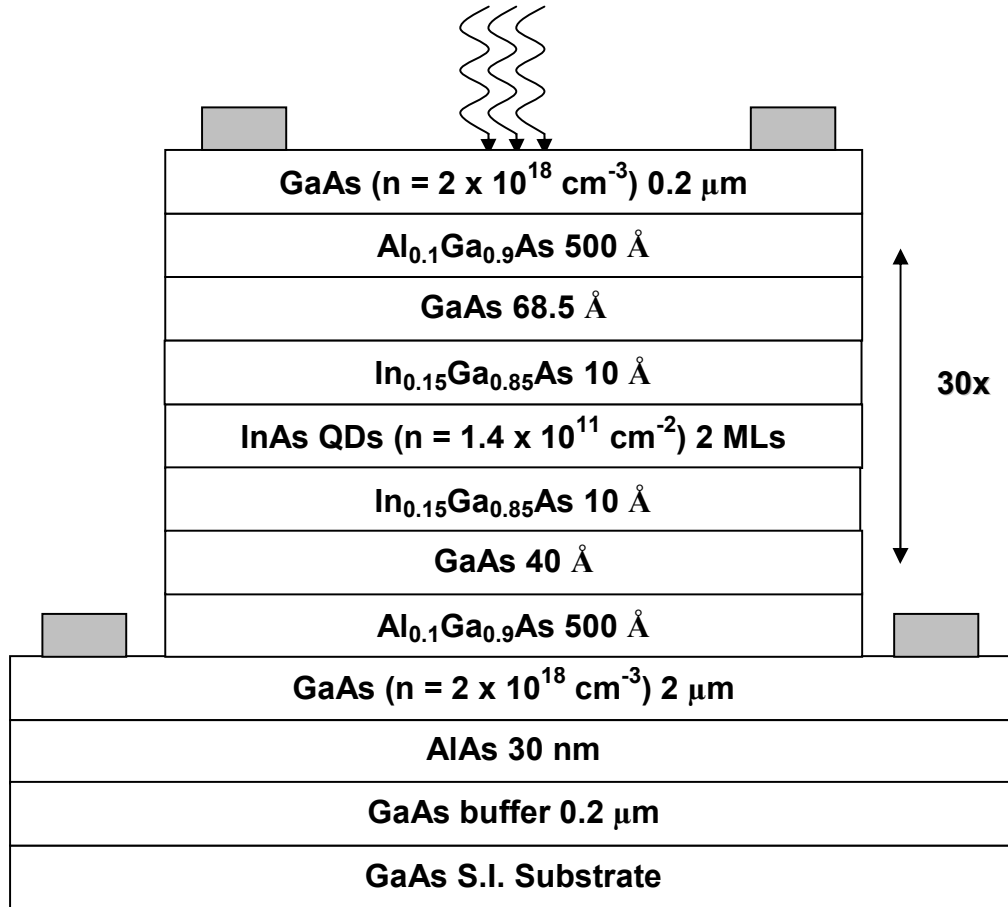
Figure 4.2: Heterostructure schematic of InAs/$In_{0.15}Ga_{0.85}As$/GaAs DWELL infrared photodetector

The density of the InAs QDs is found to be 1.4 x 10^{11} cm^{-2} from atomic force microscopy (AFM). The AFM image of the 2 MLs InAs on a 10 Å thick $In_{0.15}Ga_{0.85}As$ QW is shown in Figure 4.3. The InAs QDs are directly doped with Si at a sheet doping concentration of 1.4 x 10^{11} cm^{-2} or approximately 1 electron/dot.

QD Density – 1.4×10^{11} cm^{-2}

0.5 µm (vertical)

0.5 µm (horizontal)
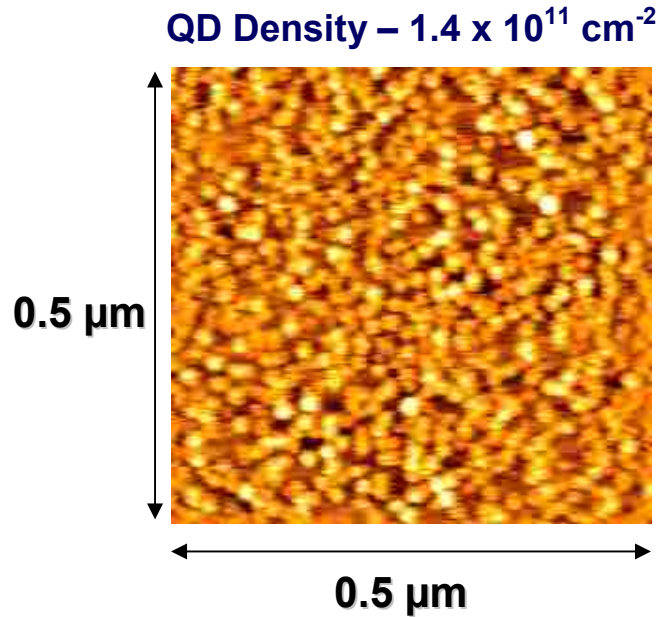
Figure 4.3: AFM Image of 2 MLs of InAs QDs on a 10 Å In$_{0.15}$Ga$_{0.85}$As QW

The InAs QDs are capped with a 10 Å thick In$_{0.15}$Ga$_{0.85}$As QW, which is the second part of the QW. Following the growth of the In$_{0.15}$Ga$_{0.85}$As QW, the remaining part of the GaAs QW which is 68.5 Å thick is grown. The growth rates used for In, Ga and Al are 0.159 ML/s, 0.9 ML/s and 0.1 ML/s respectively. After the growth of GaAs QW layer, a 180 sec growth interrupt with just As shutter open is placed to ramp the temperature from 470º C to 590º C for the Al$_{0.1}$Ga$_{0.9}$As barrier to be grown. Finally, a 0.2 µm thick n+-GaAs top-contact layer is grown at the same temperature as the barrier. The GaAs contact-layer is directly doped with Si at a doping concentration of 2×10^{18} /cm^3.

4.3   Energy Bandstructure

Figure 4.4 shows the energy band profile for the alternative DWELL structure. The conduction band offset between the ground electronic state of the InAs QD and the

$Al_{0.1}Ga_{0.9}As$ barrier is 241 meV. The band offset is calculated from the room temperature photoluminescence spectra using 60%-40% split. The room temperature PL spectrum for the 30-period $InAs/In_{0.15}Ga_{0.85}As/GaAs$ dots-in-well (DWELL) quantum dot infrared photodetector (QDIP) is shown in Figure 4.5. The PL wavelength of the InAs QDs is found to be 1080 nm. In the new design many layers can be grown without introducing dislocations which is crucial to achieve high quantum efficiency. The PL measurements were done at University of Sheffield.
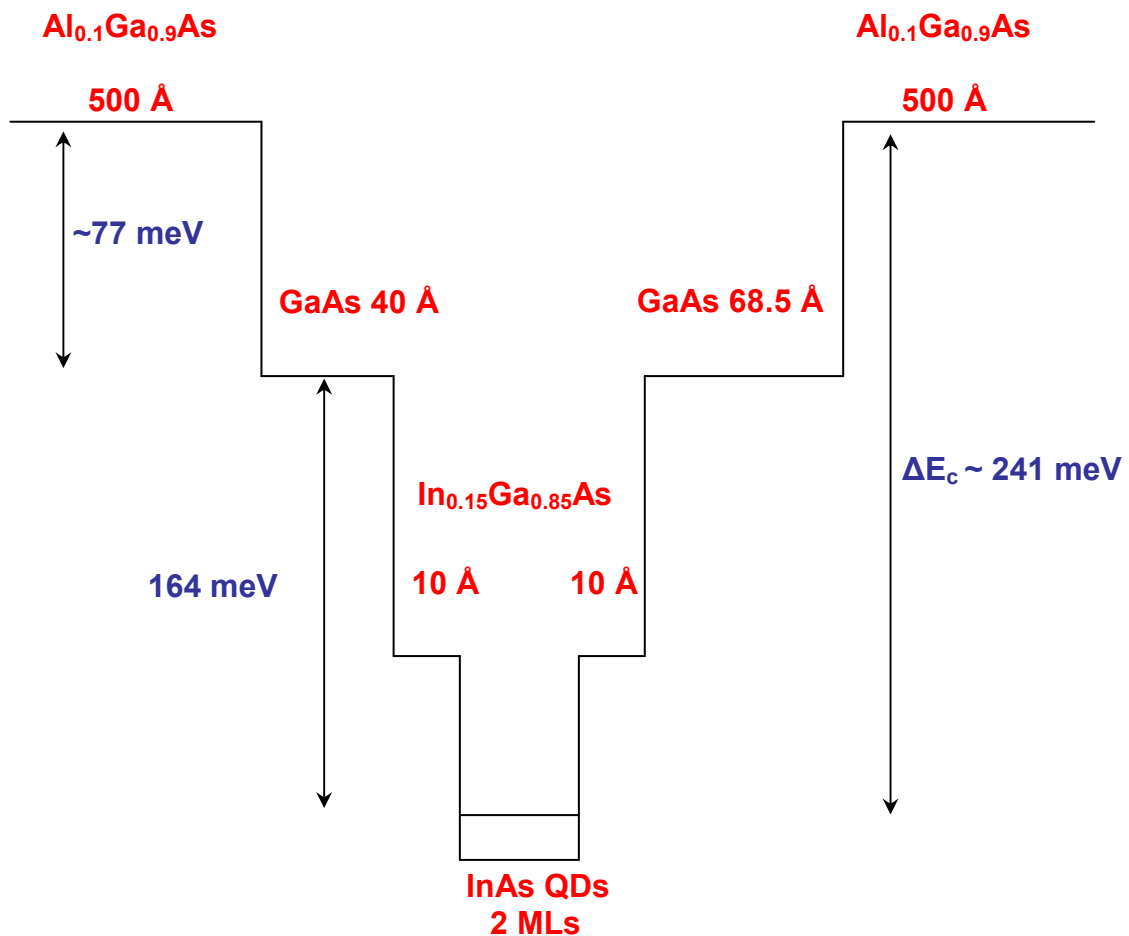
Figure 4.4: Conduction band profile of the low strain DWELL heterostructure
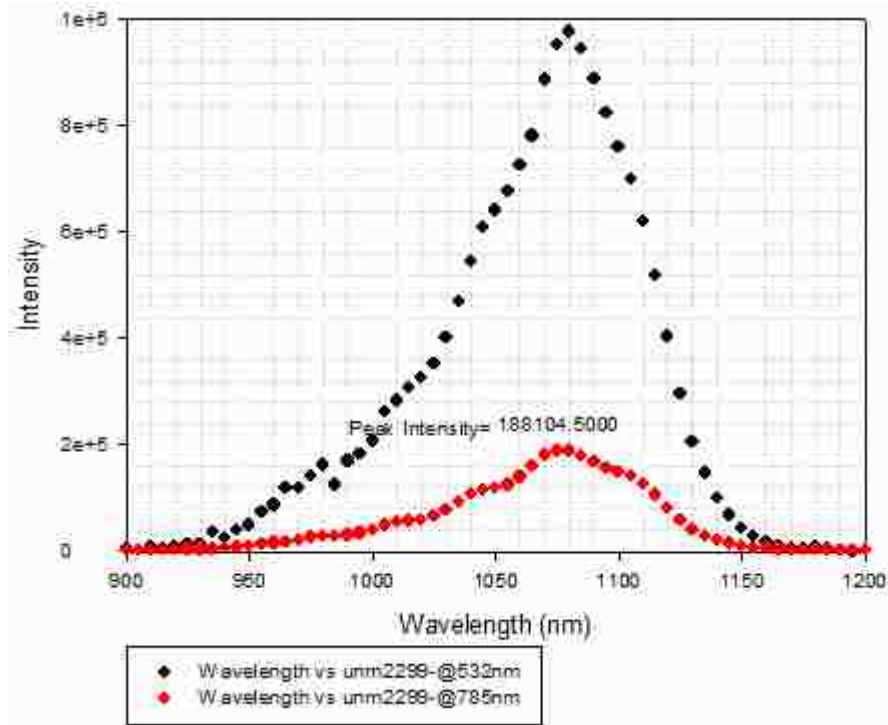
Figure 4.5: Room temperature PL of the 30-period InAs/In$_{0.15}$Ga$_{0.85}$As/GaAs DWELL heterostructure measured with two different lasers (532nm and 785 nm)

4.4 Device Fabrication

The photodetector is fabricated in a class-100 clean room where 400 μm x 400 μm mesas of the devices are defined using standard photolithography, metal deposition and dry etch techniques. First step involves defining mesas using photolithography and dry etching. After defining mesas metal deposition is used to deposit bottom and top contacts. The final step involved annealing the contacts at 400º C in a N$_2$ rich atmosphere for 45 seconds.

4.5 Device Characterization

Spectral response measurements were undertaken at 77K in a Nicolet 6700 FTIR spectrometer. The background spectrum is measured in the main compartment of the

FTIR with a Mercury Cadmium Telluride (MCT) detector which is cooled down to 77K. The spectrum from the detector is measured with the MCT detector and divided by the background. The spectral response data for the 30-period $InAs/In_{0.15}Ga_{0.85}As/GaAs$ DWELL infrared photodetector for different bias ranges is shown in Figures 4.6, 4.8 and 4.9.

a) Bias range -5 to -4 V

From the Figure 4.6 it can be observed that in the bias range -5 to -4 V there is mid-wave response around 5.25 μm (i.e. 236 meV) and long wave response around 8.35 μm (i.e. 148 meV). From PL measurements, the difference between the ground state in the InAs QD and conduction-band edge of the $Al_{0.1}Ga_{0.9}As$ barrier is estimated to be between 254 meV and 270 meV; Therefore, the 5.25 μm (~236 meV < 241 meV) and 8.35 μm (~ 148 meV < 164 meV) peaks are due to bound-to-bound (B-B) transitions from the ground state in the InAs QD to a state in the $In_{0.15}Ga_{0.85}As$ or GaAs QW. The 5.25 μm peak could probably be due to a bound-to-bound transition from the ground state in the InAs QD to a state in the GaAs QW, which is very close to the conduction-band edge of the $Al_{0.1}Ga_{0.9}As$ barrier. The 8.35 μm peak could be due to a B-B transition from the ground state in the InAs QD to a state in the $In_{0.15}Ga_{0.85}As$ QW, which is very close to the conduction band edge of the GaAs QW as shown in Figure 4.7.
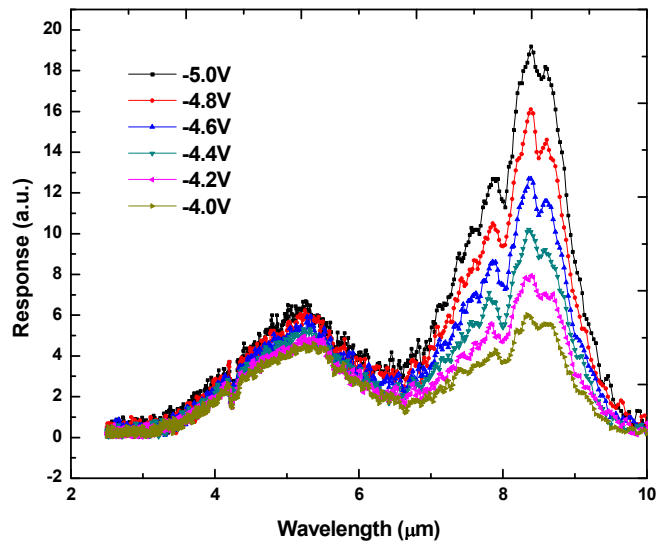
Figure 4.6: Spectral response data for the 30-period InAs/In$_{0.15}$Ga$_{0.85}$As/GaAs/Al$_{0.1}$Ga$_{0.9}$As DWELL infrared photodetector taken at 77K for bias range -5 V to -4 V
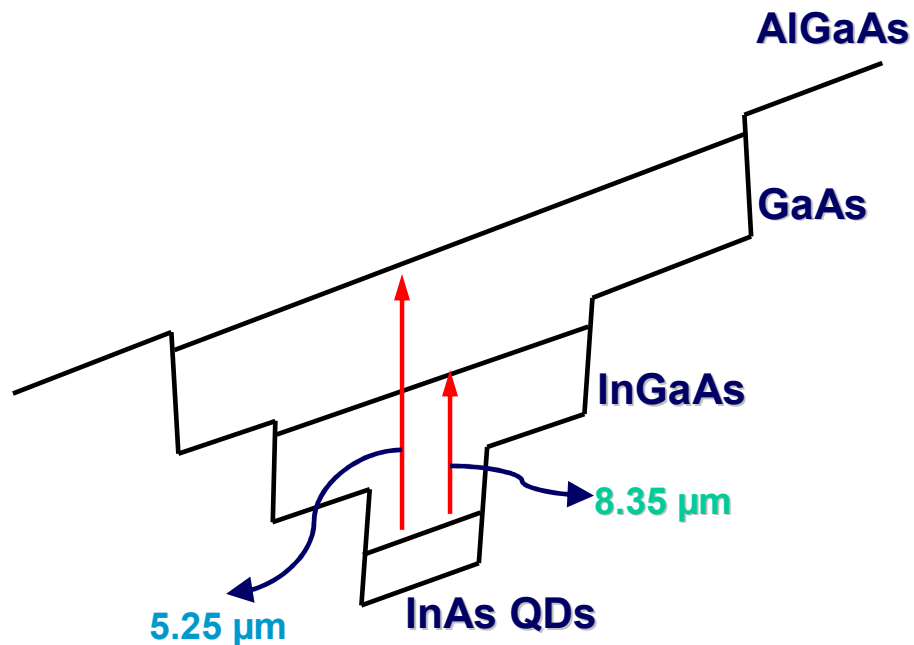

Figure 4.7: Bound-to-bound (B-B) transitions from ground state in InAs

QD to GaAs QW (~5.25 μm) and In$_{0.15}$Ga$_{0.85}$As QW (~8.35 μm)

b)   Bias range -3.8 to 0 V

In the bias range -5 to -4V, the long wave response at 8.35 µm dominates over the
mid wave response. As the bias is decreased from -3.8 to -2 V, the mid-wave response
peak starts increasing in magnitude in comparison to the long-wave response peak. In the
bias regime, -1.8 to 0 V, the mid-wave response peak dominates completely over the
long-wave response peak as shown in Figure 4.8. However, there is still some weak
response at 8.35 µm in that bias regime. This bias tunable response has been observed in
the standard DWELL detectors before and is due to the quantum confined stark effect
(QCSE) exploited by the asymmetry in the bandstructure [4].
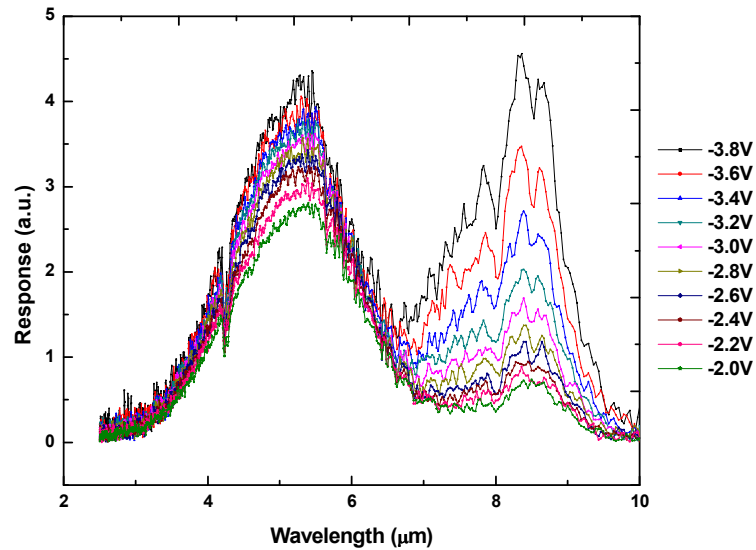
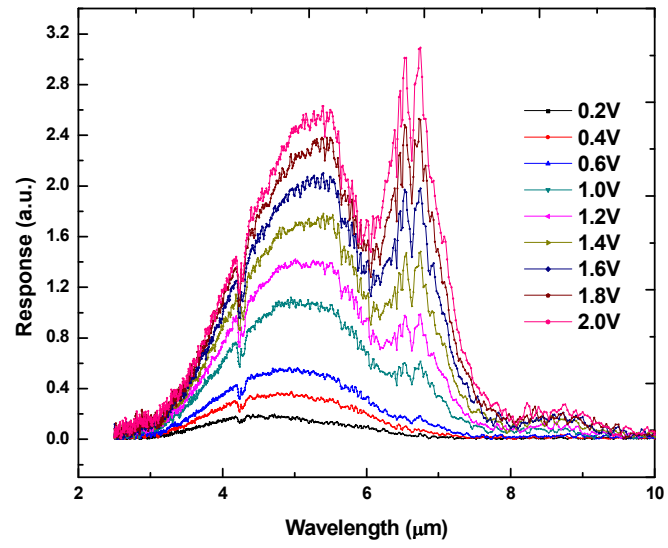**(a)**
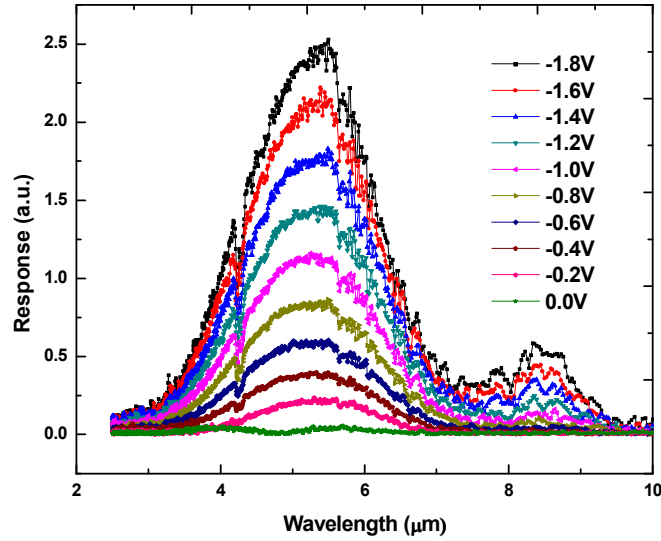
(b)

Figure 4.8: Spectral response data for the 30-period InAs/In$_{0.15}$Ga$_{0.85}$As/GaAs/Al$_{0.1}$Ga$_{0.9}$As DWELL infrared photodetector taken at 77K for bias range: (a) -3.8 V to -2 V (b) -1.8 V to 0 V.

c)   Bias range 0.2 to 5 V

From 0.2 – 0.4 V, the peak response is at 5.25 μm and from 0.6V we can see the 6.5 μm response increasing with bias and becomes comparable to the 5.25 μm peak. From 2.2 to 5 V onwards, the 6.5 μm response is the dominant peak response; moreover, from 4.2 to 5V onwards, there is very weak response at 8.9 μm as shown in Figure 4.9. The 6.5 μm (~191 meV) peak could be a bound-to-bound transition from the ground state in the InAs QD to a state in the GaAs QW as shown in Figure 4.10.

(a)
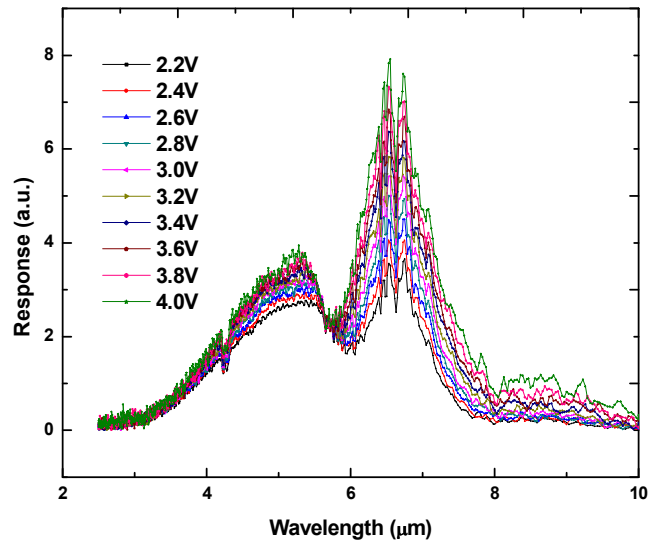
(b)

(c)

Figure 4.9: Spectral response data for the 30-period InAs/In$_{0.15}$Ga$_{0.85}$As/GaAs/Al$_{0.1}$Ga$_{0.9}$As DWELL infrared photodetector taken at 77K for bias range: (a) 0.2 V to 2 V (b) 2.2 V to 4 V (c) 4.2 V to 5 V.
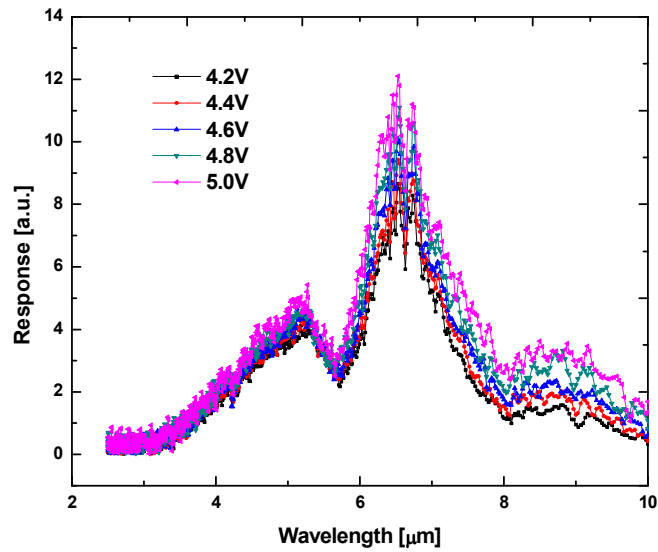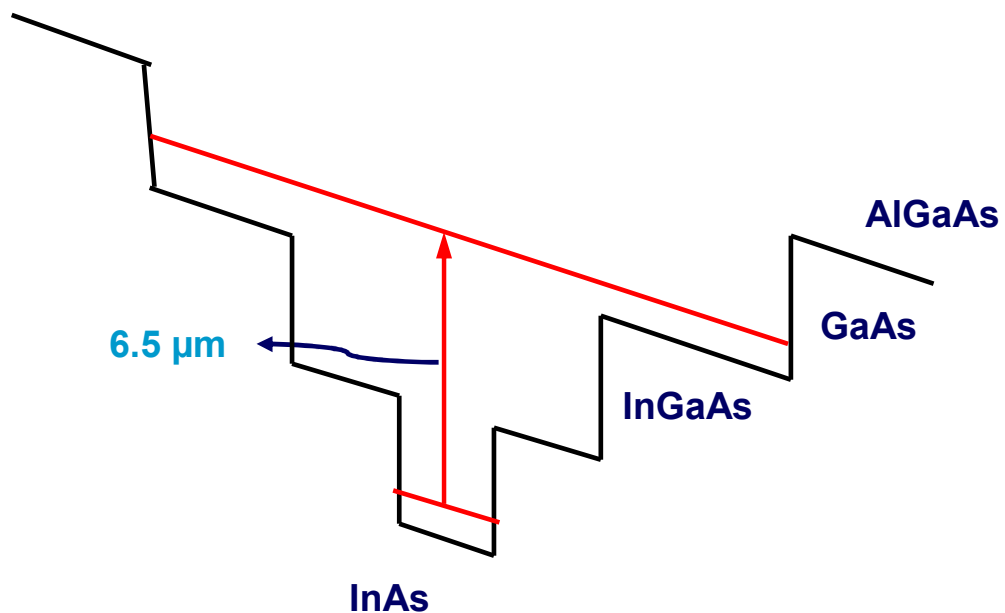

Figure 4.10: Bound-to-bound (B-B) transitions from ground state in InAs

QD to a state in GaAs QW (~6.5 μm)

The photocurrent density is measured at 77K using an aperture (F# = 1.34) with a 40º field of view seeing a quartz window at T=300K. The dark current density is measured at 77K with a cold shield blocking the field of view. Figure 4.11 shows the plot of dark current and photocurrent densities versus normalized mean electric field. The electric field is derived by dividing the thickness of the detector with bias and then normalized by dividing with the maximum electric field. From the plot it can be seen that the photocurrent density is higher than the dark current density of the device from which it can be inferred that the detector is background limited at 77K.
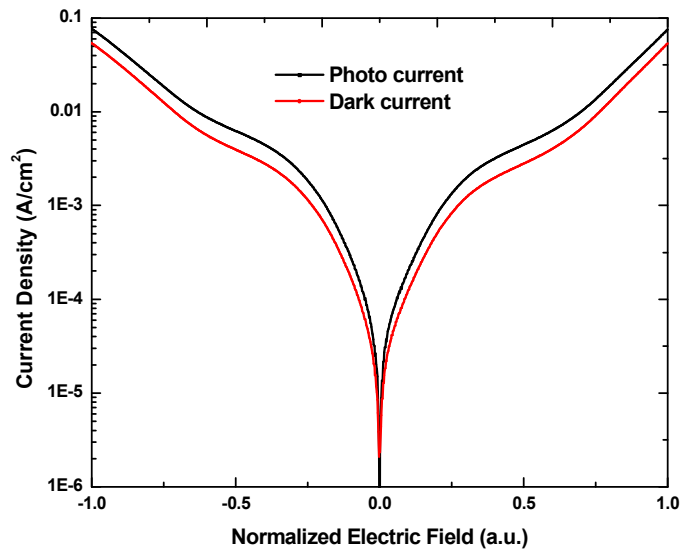
Figure 4.11: Photocurrent and dark current densities for the 30-period InAs/In$_{0.15}$Ga$_{0.85}$As/GaAs DWELL infrared photodetector measured at 77K for bias range -1 to 1 V

Calibrated radiometry measurements were undertaken using a 700K blackbody and an optical chopper to determine the peak responsivity of the detectors at T=77K. The details of the responsivity setup and how the responsivity is derived are discussed in

Chapter 2. Figure 4.12 shows the plot of peak responsivity with different bias. The responsivity increased with bias as expected as the signal from the device increased with bias. The highest peak responsivity measured at 77K is 0.37 A/W at -5V at 8.35 μm and the responsivity at 5V at a wavelength of 6.5 μm is 0.17 A/W.
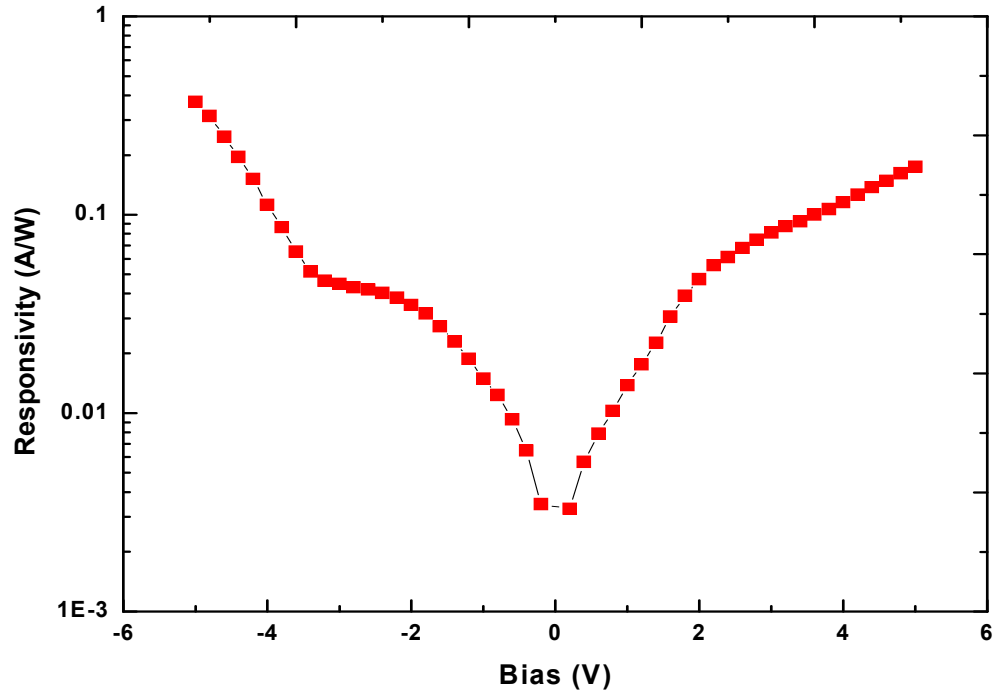
Figure 4.12: Peak responsivity for the 30-period InAs/In$_{0.15}$Ga$_{0.85}$As/GaAs DWELL infrared photodetector measured at 77K for bias range -5 V to 5 V

Noise current density of the sample is measured at 77K with a SRS 550 fast fourier transform (FFT) analyzer under the same conditions as the photocurrent density. The measured noise current density with change in bias is displayed in Figure 4.13. As expected the noise current density increased with bias due to the increase in dark current density. The lowest noise current density is at 5.51 x 10^{-14} A/Hz$^{1/2}$ measured at 0 V bias.

The photoconductive gain is the fraction of thermally or photogenerated carriers that reach the collecting contacts [5]. The photoconductive gain is derived from the total current (i.e. sum of the photocurrent and dark current) and the noise current density as follows:

$$Photoconductive\ gain = \frac{i_n^{\,2}}{4qI_{dc}\Delta f},$$

where $i_n/\sqrt{\Delta f}$ is the noise current density, I_{dc} is the total current, q is the charge of the electron, and Δf is the frequency bandwidth. The noise current density and the total current are measured under the same conditions as described earlier. The derived photoconductive gain is shown in Figure 4.14. The highest gain is 1.55 at a bias of -5 V and T=77K. The gain is lower than the values reported in literature for standard QDIPs and might be lower due to the carrier recombination processes dominating in the detector.

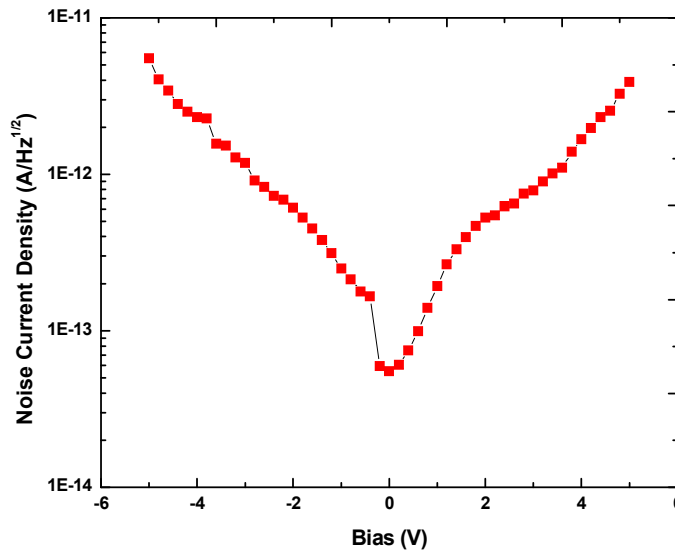**Figure 4.13: Noise current density for the 30-period InAs/In$_{0.15}$Ga$_{0.85}$As/GaAs DWELL infrared photodetector measured at 77K for bias range -5 V to 5 V**

QE is the ratio of number of free electron-hole pairs generated and collected by the number of incident photons. QE is derived from peak responsivity (R_p) and the photoconductive gain (g) as follows:

$$Quantum\ Efficiency = \frac{hcR_p}{gq\lambda_p},$$

where λ_p is the peak wavelength at the particular bias, h is the planck's constant and c is the speed of light. The plot of the derived QE is shown in Figure 4.15. The highest QE is 4.4% at a bias of -4.8 V and T=77K. The reported QE is comparable to that obtained in QWIPs.

Figure 4.14: Photoconductive gain for the 30-period InAs/In$_{0.15}$Ga$_{0.85}$As/GaAs DWELL infrared photodetector measured at 77K for bias range -5 V to 5 V
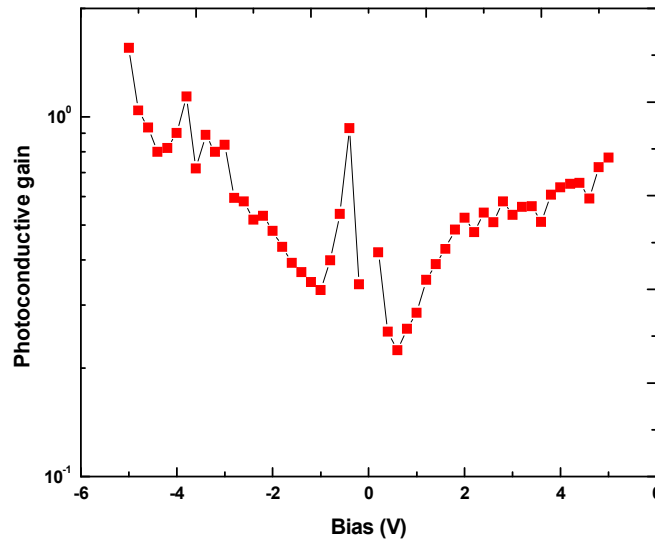
Figure 4.15: QE for the 30-period InAs/In$_{0.15}$Ga$_{0.85}$As/GaAs DWELL infrared photodetector measured at 77K for bias range -5 V to 5 V
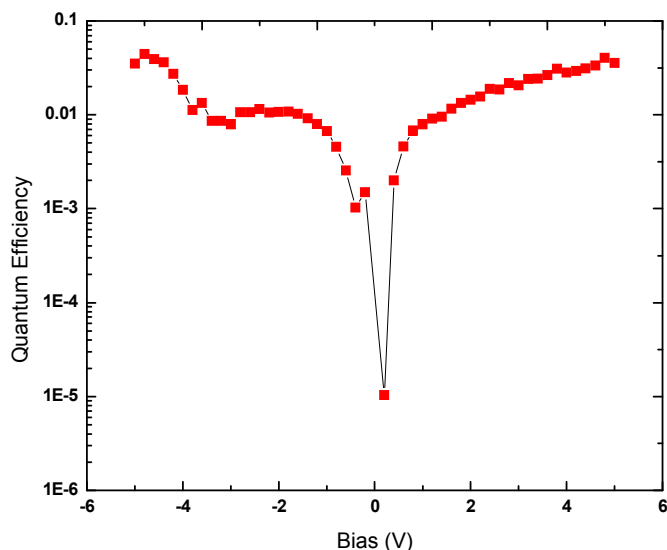
The peak detectivity values are plotted and displayed in Figure 4.16. The peak detectivity of the sample is derived from the peak responsivity, area of the aperture and noise current density as discussed in Chapter 2. The highest value of peak detectivity is 3.1 x 10^9 cm Hz$^{1/2}$/W at 2.6 V and T=77K. Even though the peak responsivity is highest at a bias of -5 V, as D* is a measure of signal to noise ratio the optimal ratio is found to be at a bias of 2.6 V at a peak wavelength of 6.5 μm. The D* value is at least an order of magnitude lower than values reported for QWIPs. The reason for low D* is due to low photoconductive gain and quantum efficiency. The D* can be improved by decreasing the thickness of the AlGaAs barriers which may increase the overall collection efficiency. The D* may also be improved by increasing the Si doping concentration of the InAs quantum dots to 2e/dot which will increase the fraction of carriers reaching the collecting contacts and, therefore, will increase the gain. An optimal combination of barrier

thickness and doping concentration needs to be found to enhance the performance of these devices. Also, more number of DWELL layers might improve the performance, and, therefore, needs to be investigated.
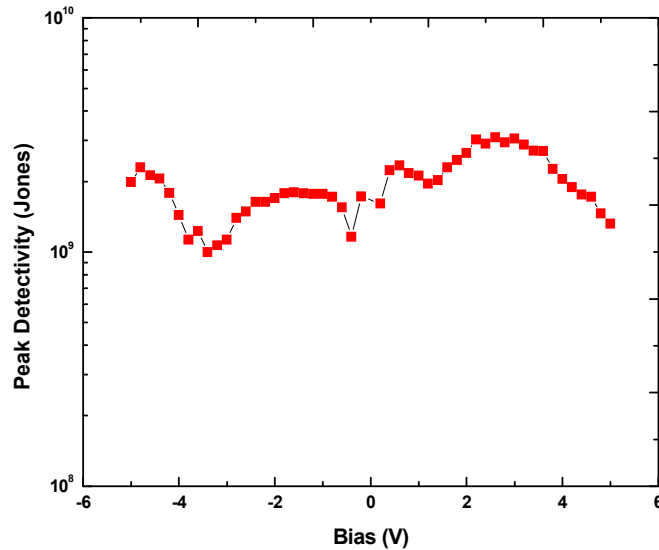
Figure 4.16: Peak detectivity for the 30-period InAs/In$_{0.15}$Ga$_{0.85}$As/GaAs DWELL infrared photodetector measured at 77K for bias range -5 V to 5 V

4.6 Conclusions

A low strain alternative DWELL detector to the standard InAs/In$_{0.15}$Ga$_{0.85}$As DWELL infrared photodetector is designed and fabricated. A greater number of DWELL layers can be grown based on this design without inducing dislocations due to its low strain. A 30-period InAs/In$_{0.15}$Ga$_{0.85}$As/GaAs DWELL infrared photodetector based on the new design has been grown, fabricated and characterized. A responsivity of 0.37 A/W is measured at a bias of -5 V for a peak wavelength of 8.35 μm. A gain of 1.55 at a bias of -5 V and quantum efficiency of 4.4% at a bias of -4.8 V has been measured. The highest detectivity measured for the sample is 3.1 x 10^9 cmHz$^{1/2}$/W at a bias of 2.6 V for

a peak wavelength of 6.5 µm. Based on the results this alternative DWELL design is a promising technology for quantum dot infrared photodetectors.

[1] R. Kaspi and K. R. Evans, Appl. Phys. Lett. 67, 819 (1995).

[2] A. Stintz, G. T. Liu, A. L. Gray, R. Spillers, S. M. Delgado, and K. J. Malloy, J. Vacc. Sci. Tech. B, 18(3), May/June 2000.

[3] J.I. Chyi, T.E. Nee, C.T. Lee, J.L. Shieh, and J.W. Pan, J. Cryst. Growth 175/176, 777 (1997).

[4] Unal Sakoglu, J. Scott Tyo, and Majeed M. Hayat, J. Optical. Soc. Am. B. 21(1), 2004.

[5] Sunil Raghavan's thesis, intersubband quantum dots-in-well infrared photodetectors, University of New Mexico, August 2003.

Chapter 5

Conclusions and Future Work

In this work, various methods to improve the performance of the quantum dots-in-well infrared photodetector have been investigated. The motivation behind this work is to improve the D* and operating temperature of the DWELL infrared photodetectors. The doping of the QDs is one of the most important design parameters for QDIPs, primarily because of its relation to dark current and noise. It has been proved that as the doping increases, so does the dark current and noise.

In Chapter 2, investigation to find the optimal doping for InAs/In$_{0.15}$Ga$_{0.85}$As DWELL infrared photodetectors has been reported. Five samples: A (undoped), B (0.75 x 10^{10} cm^{-2}), C (1.5 x 10^{10} cm^{-2}), D (3 x 10^{10} cm^{-2}) and E (6 x 10^{10} cm^{-2}) with increasing sheet doping concentrations were grown and tested. From the results, it was concluded that 3 x 10^{10} cm^{-2} is the optimum doping for these detectors. The sample D, which has been doped to the optimum doping concentration, has the highest responsivity (i.e. 0.32 A/W at 1.6 V) and detectivity (i.e. 8 x 10^{10} jones at 1.6 V) compared to the other samples. The BLIP temperature which is an optimum measure of signal-to-noise ratio agrees with the detectivity data. Sample D has the highest BLIP temperature (91K) among all the samples.

In addition, Sample D has the highest magnitude of spectral response compared to all other samples. It has been observed that the magnitude of spectral response and the photocurrent density increase with the amount of Si-doping concentration in the QDs. A drop in spectral response and photocurrent density has been observed for Sample E. The

reason behind the decrease in spectral response could be due to occupancy of higher lying excited states. The residual doping from the InAs/In$_{.15}$Ga$_{.85}$As layers may provide additional carriers that occupy the ground state. It is estimated that the background sheet doping concentration for bulk InAs to be 1.2×10^9 cm^{-2}.

In this doping study, the upper part of the QDs are directly doped with Si atoms, which means the In, As and Si shutters are open simultaneously. Future work could include modulation doping of the QDs, which can be achieved by doping the In$_{0.15}$Ga$_{0.85}$As QWs or GaAs barriers.

Even though the optimum sheet doping concentration of the InAs/In$_{0.15}$Ga$_{0.85}$As DWELL QDIPs has been determined, the detectors still suffer from low operating temperatures and detectivity compared to the state of the art detectors. This can be attributed to the low QE of the DWELL-based detectors. Normally, only a single pass of light gets through the detector active region and emerges out through the substrate. One of the ways to improve QE is by forcing multiple passes of light through the detector active region, which can be achieved by placing the DWELL layers in a resonant cavity (RC-DWELL) surrounded by photon reflectors (e.g. DBRs). Chapter 3 discussed the performance enhancement of the InAs/In$_{0.15}$Ga$_{0.85}$As DWELL-based detectors by using the RC-DWELL structure.

The RC-DWELL sample was designed for a resonant wavelength of 9.5 μm. The resonant wavelength has been verified with spectral response and reflectivity measurements of the cavity and the DBR mirror. The QE increased (i.e. 10%) significantly compared to the standard DWELL sample (i.e. 1.25% at 10 μm). A factor of six increase in photocurrent density has been measured compared to the standard

DWELL detectors at V_b=2.1V and 80 K. Similarly, the responsivity increased by a factor of six and the detectivity increased by a factor of three, at 1.2V and 77K. The measured peak responsivity of the RC-DWELL detector is 0.76 A/W at 1.4V applied bias and the peak detectivity was 1.4 x 10^{10} cm $Hz^{1/2}$/W at 0.5V. Therefore, it can be concluded that the resonant cavity has significantly enhanced the performance of the DWELL detector due to the increase in the QE of the device.

Future work may include increase in the number of DWELL layers in the active region and a cavity that includes both top and bottom DBR mirrors. Current design of RC-DWELL detector has top mirror as air/semiconductor interface, which has only 30% reflectivity. An alternative design of top mirror may include 1-period of 757nm GaAs/ 1613 nm AlxO/ 757nm GaAs with a reflectivity of about 70%. There are some fabrication issues that need to be resolved. During the oxidation process, the active region layers are exposed to the water vapor. Even though the oxidation rate of GaAs layers is negligible, there is some evidence of oxidation of the DWELL layers based on reflectivity measurements and simulation of the cavity.

In Chapters 2 and 3, some of the ways of improving the performance of the DWELL detector have been investigated, one by optimizing the doping and the other by increasing the QE. Another way is to increase the number of DWELL layers, as it increases the absorption QE and, therefore, the net QE. As the responsivity is directly proportional to the net QE, an increase in responsivity and detectivity is also expected.

The average indium composition in the standard DWELL is about 19%, which corresponds to 1.35% compressive strain on GaAs. With such a high strain a greater number of DWELL layers cannot be grown without introducing dislocations. These

dislocations act as non-radiative recombination centers and reduce the QE of the device. In order for a greater number of DWELL layers to be grown the strain has to be reduced. An alternative DWELL structure, which has low strain compared to the standard DWELL, has been designed and discussed in chapter 4. This new DWELL structure consists of InAs QDs placed in a $In_{0.15}Ga_{0.85}As$ QW, which in turn is placed in a GaAs QW and surrounded by $Al_{0.1}Ga_{0.9}As$ barriers. The average indium composition in this new DWELL design is 5% and that corresponds to 0.35% compressive strain. A 30-stack DWELL detector based on the low strain design has been grown, processed and characterized for measuring device performance.

The spectral response measurements showed response at three different wavelengths 5.2 μm, 6.5 μm and 8.35 μm. A responsivity of 0.37 A/W is measured at a bias of -5 V for a peak wavelength of 8.35 μm for the new DWELL design. A gain of 1.55 at a bias of -5 V and QE of 4.4% at a bias of -4.8 V have been measured. The highest detectivity measured for the sample is 3.1 x 10^9 cmHz$^{1/2}$/W at a bias of 2.6 V for a peak wavelength of 6.5 μm. From the measurements, it can be concluded that the 30-stack detectors suffer from low gain, QE and responsivity. The advantage of these devices is that they have low dark current and noise current density. The D* can be improved by optimizing the design of the detector. The doping of the QDs can be increased to 2e/dot and the thickness of the barriers can be reduced to increase the collection efficiency. Also, the optimal number of DWELL layers for the detector structure needs to be investigated.

In conclusion, the overall performance of $InAs/In_{0.15}Ga_{0.85}As$ DWELL infrared photodetector has been improved by optimizing the doping and embedding the active

region in a resonant cavity. In addition, an alternative to the standard DWELL a InAs/In$_{0.15}$Ga$_{0.85}$As/GaAs DWELL detector, has been designed and tested with promising results.